Applied Energy 401 (2025) 126626

Contents lists available at ScienceDirect

Applied Energy

journal homepage: www.elsevier.com/locate/apen

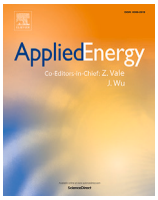

Numerical modeling and validation of an integrated module in a reversible solid oxide cell system

Shidong Zhang [a], Roland Peters [a], Nicolas Kruse [a], Robert Deja [a], Steven B. Beale [b,c,*], Remzi Can Samsun [a], Rüdiger-A. Eichel [a,d,e]

[a] Forschungszentrum Jülich GmbH, IET-1, 52425 Jülich, Germany
[b] Forschungszentrum Jülich GmbH, IET-3, 52425 Jülich, Germany
[c] Mechanical and Materials Engineering, Queen's University, Kingston ON K7L 3N6, Canada
[d] RWTH Aachen University, Institute of Physical Chemistry, Aachen, Germany
[e] RWTH Aachen University, Faculty of Mechanical Engineering, Aachen, Germany

HIGHLIGHTS

- Presents novel model for solid oxide cell integrated module.
- Model covers both fuel cell and electrolysis modes.
- Comparison with experimental results shows very good agreement.
- Provides a tool for accurate representation of integrated systems.
- Contributes to the advancement of the technology for industrial applications.

ARTICLE INFO

Keywords:
Modeling
Fuel cells
Electrolyzers
Computational fluid dynamics
Solid oxide cells
Electrochemical stacks

ABSTRACT

This study presents an advanced numerical modeling approach for analyzing a 10/40 kW reversible solid oxide cell Integrated Module designed by Forschungszentrum Jülich GmbH. The present authors extend the distributed resistance analogy method using OpenFOAM to comprehensively simulate the complex physical processes within the sub-components of the Integrated Module. The model incorporates numerical techniques, including the arbitrary mesh interface for sub-component interpolation, a radiative heat transfer model for inter-component heat exchange, and a region-to-region coupling approach for surface and volume temperature coupling. Numerical predictions demonstrate good agreement with experimental measurements in both fuel cell and electrolysis modes, with maximum temperature deviations of 10–15 K observed in the middle parts of the sub-stacks. The model successfully captures the uniform performance across sub-stacks and the high efficiency of the heat exchangers. Analysis of species and current density distributions confirms that the design ensures uniform sub-stack operation, which is crucial for long-term performance. While discrepancies between predicted and reference temperatures in the heating plates are within acceptable limits, the study highlights the potential limitations of simple models in representing real-world systems. This research provides valuable insight into the Integrated Module behavior, enabling informed design optimization and operational strategies. The developed methodology offers a powerful tool for rapid and accurate characterization of reversible solid oxide cell systems, contributing to the advancement of reversible solid oxide cell technology as it scales up for industrial applications.

1. Introduction

The global energy landscape is experiencing a significant transformation as efforts to combat climate change and enhance energy security intensify. A central aspect of this transition is the move towards cleaner, more sustainable energy resources. In this regard, low-emission hydrogen has emerged as a key solution for decarbonizing sectors where emissions are particularly difficult to reduce. Additionally, recent global

* Corresponding author at: Forschungszentrum Jülich GmbH, IET-3, 52425 Jülich, Germany.
Email address: s.beale@fz-juelich.de (S.B. Beale).

https://doi.org/10.1016/j.apenergy.2025.126626
Received 3 April 2025; Received in revised form 12 June 2025; Accepted 7 August 2025
Available online 26 August 2025

Nomenclature

Abbreviations

AMI	Arbitrary mesh interface
CFD	Computational fluid dynamics
DRA	Distributed resistance analogy
HEX	Heat exchanger
HPL	Heating plate
IM	Integrated Module
PID	Proportional integral derivative
SOC	Solid oxide cell

English

$\boldsymbol{A}$	Coefficient matrix (-)
$\boldsymbol{b}$	Source term vector (-)
$\boldsymbol{F}_D$	Resistance term (N m^{-3})
$\boldsymbol{i}''_{\mathrm{E}}$	External current density due to Nernst potential (A m^{-2})
$\boldsymbol{r}$	Diffusion or conduction vector (-)
$\boldsymbol{u}$	Superficial velocity (m s^{-1})
A	Matrix coefficient (-)
b	Source term (-)
C_p	Specific heat (J kg^{-1} K^{-1})
d	Distance (m)
D^{eff}	Effective diffusion coefficient (m^2 s^{-1})
k	Thermal conductivity (W m^{-1} K^{-1})
p	Pressure (Pa)
Q	Heat source/sink (W m^{-3})
q_{r}	Radiative heat flux (W m^{-2})
R	Mass source/sink (kg s^{-1} m^{-3})
T	Temperature (K)
V	Electric potential (V)
y_{k}	Mass fraction of species k (-)

Greek

α	Heat transfer coefficient (W m^{-3} K^{-1})
γ	Volume fraction (-)
ρ	Mixture density (kg m^{-3})
σ	Electric conductivity (S m^{-1})
σ_{B}	Stefan-Boltzmann constant (W m^{-2} K^{-1})
ε	Emissivity (-)

energy issues have further emphasized the role of low-emission hydrogen in strengthening energy security [1]. Despite increasing awareness of environmental concerns, fossil fuels such as coal, oil, and natural gas continue to dominate the global energy mix, contributing substantially to overall energy consumption. This reliance on carbon-intensive sources has resulted in numerous critical challenges, including climate change, air pollution, resource depletion, and environmental degradation. In response, there is a growing global commitment to shift towards clean and renewable power production [1]. As part of the broader goal of achieving carbon-neutral or even carbon-free energy systems, the role of clean alternatives, such as solar and wind energy, has become increasingly apparent. Additionally, electrochemical devices that facilitate the conversion of electricity to chemical energy in various energy carriers, and vice versa, are gaining prominence in the energy transition [2]. These devices play crucial roles across various sectors, including energy storage, grid flexibility, high-efficiency energy conversion, fuel flexibility, road transportation, heavy-duty vehicles, and auxiliary power units.

Solid oxide cells (SOCs) are notable among electrochemical devices for their versatility and high efficiency, primarily due to their relatively high operating temperatures, ranging from 600 °C to 1000 °C. Their ability to operate in multiple modes (fuel cell, electrolysis, and reversible) is critical in the transition to clean energy [3]. Key characteristics of SOCs include:

1. High electrical efficiency, typically between 60–65 % (based on lower heating value) in fuel cell mode, with combined heat and power efficiencies reaching 85–90 % [4]
2. High-efficiency potential in electrolysis mode, since part of the energy can be supplied in the form of heat to reduce the electrical input, e.g., utilizing excess heat from industrial processes [5]
3. Flexibility in fuel use, allowing the use of hydrogen, natural gas [6], ammonia [7], and biogas
4. Water management is not an issue as it is in low-temperature proton exchange membrane fuel cell systems
5. The potential for cogeneration, which enhances overall system efficiency
6. Scalability, making SOCs suitable for applications ranging from small portable units to large-scale power plants [5], for example, grid balancing and energy storage: when operating in fuel cell mode, the SOC generates electricity from hydrogen, natural gas, or other fuels, making it ideal for power generation. When operating as an electrolyzer, the SOC can convert excess electrical energy into hydrogen or other fuels, providing a solution for energy storage and grid balancing.

In the pursuit of optimizing SOC performance, multiphysics numerical modeling has become an important approach to capture the complex interactions within these devices. While computational fluid dynamics (CFD) methods form the foundation for simulating flow and transport phenomena, modern SOC modeling often extends beyond classical CFD to incorporate coupled electrochemical, thermal, and mass transport processes, so that researchers can gain valuable insights into the behavior of these cells, facilitate innovation, and contribute to the development of more efficient and durable SOC technologies [8]. As computational power continues to increase, tools such as OpenFOAM, originally developed for CFD, have been adapted to solve such multiphysics problems [9].

SOCs are generally implemented in stacks comprising numerous repeating units. For these stacks to function effectively, a range of auxiliary components must work in unison under specific control strategies. As a result, SOC stacks cannot be viewed as independent systems, as the performance of a given system is often heavily influenced by the supporting components. Fig. 1 displays a reversible SOC (rSOC) system developed by Forschungszentrum Jülich GmbH, capable of providing a net power of up to 13 kW in fuel cell mode (including power consumption of all supporting components and inverter losses) and operating at a net power of up to 50 kW in electrolysis mode [10]. It has demonstrated overall performance exceeding the nominal (design) power targets of 10 kW in fuel cell mode and 40 kW in electrolysis mode. The system's core element is an integrated module (IM) [11], which includes air and fuel heat exchangers (HEXs), baffle zones, insulation layers, electric heating plates (HPLs), and four sub-stacks (each consisting of 20 repeating units, with about 320 cm^2 active cell area per repeating unit). Additional components, such as a diaphragm compressor, condenser, water separator, and steam generator (for electrolysis), are essential for proper system functionality. Several studies have analyzed the performance and operation of this system [12–16]. While experimental research generally evaluates the overall system performance, numerical simulations can offer deeper insight into stack and system behavior. Previous CFD studies have mainly focused on individual repeating channels [17,18], repeating units, or single stacks. However, comprehensive modeling of complete systems remains a challenge due to computational demands. A number of studies [19–21] have utilized multiphysical modeling to

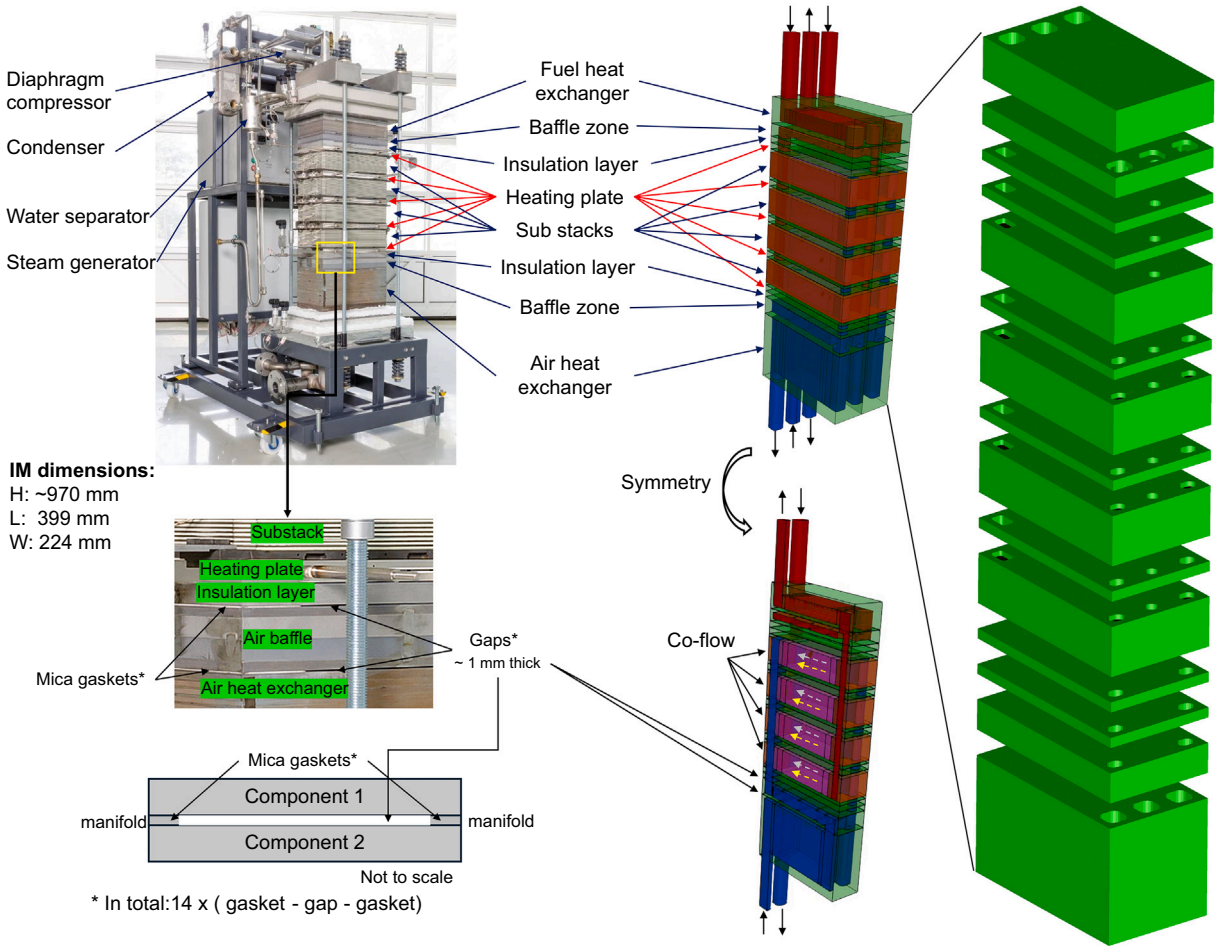

Fig. 1. The 10/40 kW reversible solid oxide cell (rSOC) system as described by Ref. [10] and the computational domain used in this study. The integrated module is approximately 970 mm tall. Each pair of components is separated by a specific gap and supported by mica gaskets. The sub-stacks and HPLs are numbered sequentially from the bottom (air side) to the top (fuel side) below.

examine full-scale SOFC systems, employing supercomputers for time-intensive calculations. However, these simulations did not explicitly model electrochemical reactions. Recent numerical studies [22–29] have utilized 'volume-averaging' approaches or a distributed resistance analogy (DRA) [30–33,35] to model SOC stacks under various operating conditions. While these studies have improved the understanding of the multiphysical aspects of SOC stacks, they often simplified or omitted the role of other system components.

Given the complexities of system-level modeling [19–21], this study aims to introduce a numerical method that enables quicker and more accessible stack/system-level analysis. The computational domain includes the same components as the experimentally monitored IM, as illustrated in Fig. 1. The research here builds upon previous work [33] by incorporating all these components simultaneously, expanding the scope of earlier studies that focused only on sub-stacks and HPLs. To enhance computational efficiency, this study also introduces additional numerical methods, such as arbitrary mesh interface (AMI) interpolations between meshes from different components, a simple thermal radiation model, and a region-to-region coupling approach. Numerical simulations of SOC operations in both fuel cell and electrolysis modes were performed, and the results were compared with other numerical simulations and experimental data.

SOCs are sensitive to spatial and temporal thermal variations, which influence ionic conductivity within the electrolyte, electrochemical reaction kinetics at the electrodes, and overall energy conversion efficiency. To maintain optimal operating conditions and prevent thermal variations such as overcooling or overheating, a proportional-integral-derivative (PID) controller is employed to regulate the temperature of the SOC stacks and ancillary components. This control mechanism is informed by multiple thermocouples strategically positioned throughout the IM, providing localized temperature feedback to enhance regulation accuracy. As an initial step toward a comprehensive understanding of the 3-D thermal, electrochemical, and fluid-dynamic behavior within the IM, this study focuses on steady-state operations. Accurately predicting temperature distributions is fundamental not only for validating the numerical model against experimental data but also for identifying effective strategies to mitigate thermal gradients in regions that are otherwise inaccessible to direct measurement. Therefore, this study prioritizes precise temperature modeling to enhance the reliability of computational frameworks.

2. Numerical procedure

2.1. Assumptions

1. The simulations are for steady state operations.
2. Fluid flow is in the laminar regime, and the gas mixtures are incompressible and ideal.
3. Fick's law is used for multi-component species transfer.
4. Thermal/mechanical deformation is not considered.
5. Internal thermal radiation is negligible; however, external thermal radiation between sub-components is important.

Table 1
Governing equations.

Description	Equation
Continuity	$\nabla \cdot (\rho\gamma \boldsymbol{u}) = \gamma R$
Momentum	$\nabla \cdot \left(\frac{1}{\gamma}\rho \boldsymbol{u}\boldsymbol{u}\right) = -\varepsilon \nabla p + \nabla \cdot (\mu \nabla \boldsymbol{u}) + \gamma \boldsymbol{F}_{\mathrm{D}}$
Species transfer	$\nabla \cdot (\rho \boldsymbol{u} y_{\mathrm{k}}) = \nabla \cdot (\gamma \boldsymbol{r} D^{\mathrm{eff}} \nabla y_{\mathrm{k}}) + \gamma R_{\mathrm{k}}$
Heat transfer	$\nabla \cdot (\rho C_p \boldsymbol{u} T) = \nabla \cdot (\gamma \boldsymbol{r} k^{\mathrm{eff}} \nabla T) - \gamma \sum \alpha_{\mathrm{j}} (T - T_{\mathrm{j}}) + \gamma Q$
Charge transfer	$\nabla \cdot (\sigma \nabla V) = \nabla \cdot i_{\mathrm{E}}''$

2.2. Governing equations

The governing equations have been presented in several prior publications [31,33,34]. For further details, readers are encouraged to refer to these sources. The relevant equations are provided briefly in Table 1.

In these equations, $\boldsymbol{u}$ is the superficial velocity, γ represents the volume fraction of each sub-region, and $\boldsymbol{r}$ denotes a diffusion vector due to geometric configurations. The interphase heat and mass transfer terms are also explained in detail in previous publications [36,37] and will not be repeated here. Radiative heat flux from the presumed diffuse-grey boundaries is specified as a boundary condition, rather than a heat source or sink. This will be discussed further in the following sections.

2.3. Computational subdomains

The IM, illustrated in Fig. 1, is composed of several sub-components that ensure proper system operation. These include,

- Sub stacks (4 ×): Each consisting of 20 repeating units with an active area of 4 × 9 cm × 9 cm.
- Heating plates (5 ×): Utilized to heat the stacks, especially in electrolysis mode (on both sides of each sub-stack). They are also employed during start-up and when operating at lower partial loads in fuel cell mode.
- Heat exchangers (2 ×): Facilitate heat transfer between the cold influent and hot effluent (on both the air and fuel sides).
- Baffle zones (2 ×): Redirect the stack outflow (on both the air and fuel sides).
- Insulation layers (2 ×): Prevent unnecessary heat transfer from the HPLs to the baffle zones (on both the air and fuel sides).

2.3.1. Sub-stacks

The IM incorporates the current stack design [10], which has a fuel electrode supported planar configuration, known as Mark-H2020. The assembly consists of four 20-layer sub-stacks, including components such as cells, interconnector plates, sealant material, wire mesh, and frames. Following the methodology from a previous study [33], it is assumed that local temperature variations within a single repeating unit are uniform in the through-plane direction, while the differences in the in-plane directions have to be taken into account in the model.

The surface area of the stack can be divided into distinct subzones based on their physical and geometrical properties. Fig. 2(a) illustrates this simplification process. A multiply shared space method was used in this modeling approach, allowing for the representation of different functional regions (air, fuel, electrolyte, and interconnect) within a common domain, such as the reaction zone. Within this framework, heat, mass, and charge transfer processes occur both within and between these regions. This approach significantly reduces the need for detailed geometrical representation, effectively transforming the complex stack structure into a series of simplified blocks. As a result, the computational mesh is greatly simplified, substantially reducing computational requirements while maintaining the essential physics of the system.

Fig. 2(b) illustrates the real stack design implemented in the sub-stacks. This configuration follows a window design, where each repeating unit consists of four cells. During the process of geometrical simplification, these four cells are represented by a single reaction zone. Based on the geometrical configuration, the simplified domain consists of solid zones, manifolds, transition areas, and the reaction zone. In this representation, the physical domains, namely air, fuel, interconnect, and electrolyte, are assembled from these sub-zones. The sub-stacks are generated by extruding the two-dimensional surface geometry along its normal direction with specified thicknesses.

2.3.2. Heat exchangers

Fig. 3(a) shows the air and fuel HEXs used in the IM. These HEX assemblies consist of 3 layers for the fuel side and 13 layers for the air side. Each layer is made up of two channel plates with a separation plate in between. The channel plate design includes 64 individual channels, with alternating layers having inverted orientations to enable counter-flow between hot and cold fluids. The dimensions of the flow ducts are also shown in the figure.

Due to the high computational resources needed to resolve all geometrical details, the authors use the DRA to improve computational efficiency. This method, first proposed by Patankar and Spalding [38] for shell-and-tube heat exchangers, as an alternative to so-called 'presumed flow methods', assigns flow resistance and heat transfer coefficients to the ducts while solving for superficial flow within them. The DRA method involves a local volume averaging approach, where the flow ducts are treated as resistance zones [34]. The surface heat transfer between the flow and the solid can therefore be treated as volumetric or interphase heat transfer, with detailed information available in previous publications [22,31,33,39]. These zones allow bidirectional flow in a counterflow setup. By applying these simplifications to all domains except for fluid/manifolds where detailed equations of motion are solved and solid zones in the through-plane direction, a significant reduction in computational complexity is achieved. This approach maintains all the essential physics of the HEXs while greatly reducing the computational resources needed for simulation.

2.3.3. Other components

The geometric simplifications in this model mainly apply to the sub-stacks and HEXs, largely due to their complex designs, which pose challenges for detailed simulations. For other components, as shown in Fig. 3(b), this study has retained the original detailed designs in the numerical calculations.

The baffle zones, present in both air and fuel pathways, redirect the outflows from the sub-stacks to the HEXs. This design enhances heat transfer from the hot exhaust gases to the cold inlet gases, improving thermal efficiency. The system was developed to minimize parasitic losses and maximize efficiency. Therefore, the flow resistance in these regions is minimal, resulting in negligible pressure losses. Given the straightforward flow characterization in these areas and their impact on heat transfer calculations, the authors have retained the original geometrical configuration of the baffle zones in this model. It should be noted that further simplifications could be applied to the baffle zones, provided their primary function is flow redirection.

The heating plates serve two purposes: they help warm up the system from a cold start and provide additional heating during electrolysis operations below the thermoneutral voltage. These plates contain electrical heating wires within the heating zone. The assembly consists of alternating layers, specifically 5 HPLs interspersed with 4 sub-stacks. This multi-layered configuration integrates heating elements and electrochemical units, facilitating thermal interactions while maintaining optimal stack performance.

Insulation layers are strategically positioned between the baffle zones and HPLs to minimize heat transfer and maintain thermal stability. The insulation material is divided into four separate blocks, effectively limiting thermal exchange between baffle zones and HPLs. This configuration plays a critical role in sustaining the stack temperature within an optimal range by mitigating radiative heat losses, particularly during endothermic electrolysis processes.

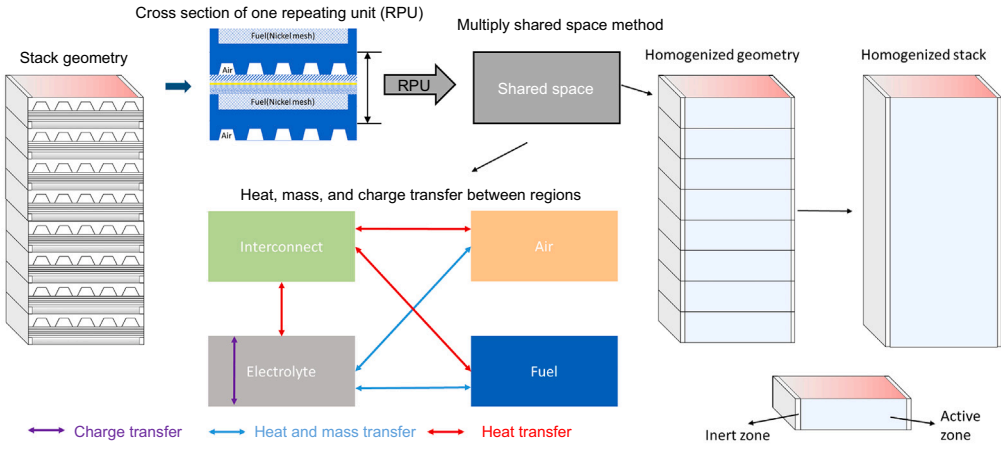

(a) Volume averaging approach employed in sub-stacks. Readers can refer to Ref. [33] for further information about the methodology.

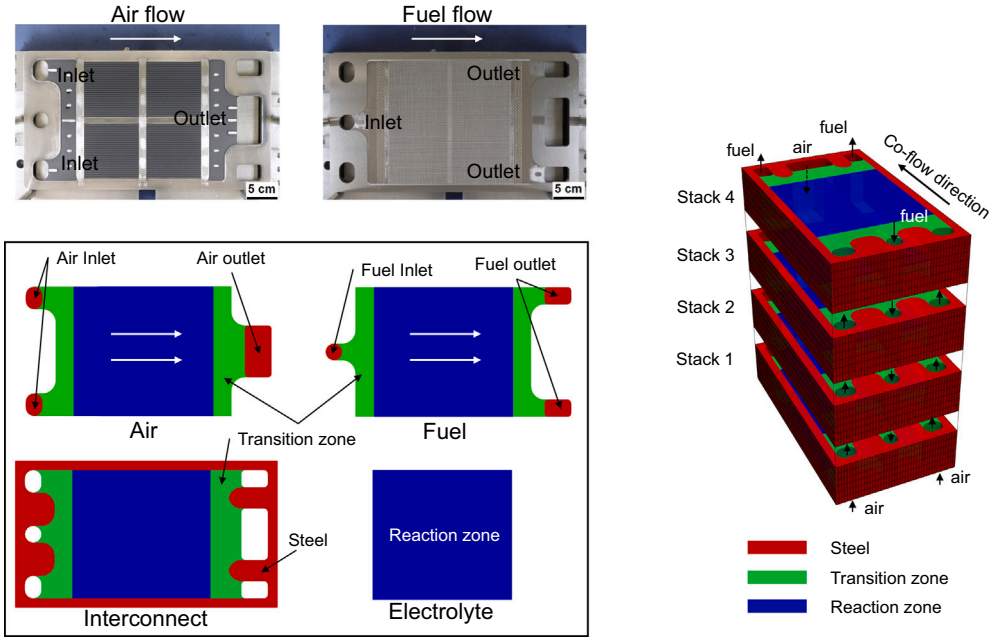

(b) The stack design incorporates the actual geometry of the flow domains for both air and fuel. In the simplified representation, distinct regions are designated for air, fuel, interconnects, and electrolytes. The simplified stack model comprises four sub-stacks, encompassing a total of 80 repeating units.

Fig. 2. Sub-stacks to be considered in the present study.

2.3.4. Assembly

The sub-components are integrated in a compact configuration, as shown in Fig. 1. This design allows for scalability in applications requiring higher power output. During assembly, the components are positioned with minimal direct contact to reduce stress from thermal expansion and unnecessary heat conduction. As depicted in Fig. 1, an intercomponent spacing of approximately 1 mm is maintained. Mica gaskets are used at the manifold zones to ensure gas-tight sealing and provide structural support for the sub-components. These mica gaskets, with their low thermal conductivity, act as thermal barriers. The gaps make radiative heat transfer between components an important factor in the thermal behavior of the IM that should not be neglected.

By employing the geometrical symmetry of the IM, the computational domain has been reduced by half to improve numerical efficiency. Fig. 4 shows all regions included in the current numerical simulations. The flow directions of air and fuel are also indicated. The sub-stack zones have a complex physical structure with the cell zone numerically shared by air, fuel, electrolyte, and interconnect regions. The 'HEX' zones feature air and fuel alongside component regions. The computational domain in this study consists of 0.39 million elements, significantly reducing mesh complexity compared to previous studies [20,21], which used meshes with about 12 million elements for a smaller SOFC system with lower power output. This substantial decrease in element count highlights the enhanced computational efficiency achieved in the current study.

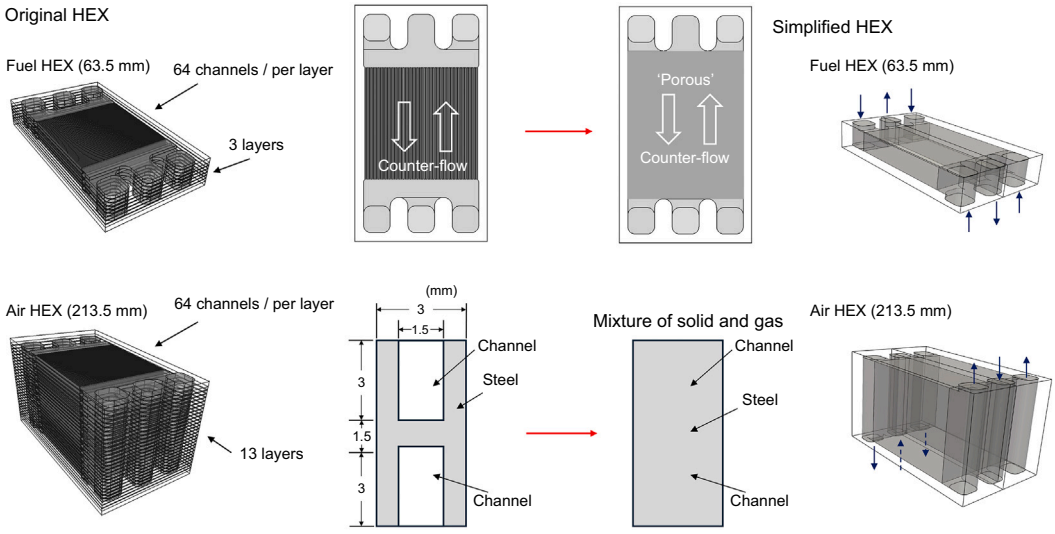

(a) The simplifications of air/fuel HEXs. After simplification, the 'porous' block allows both inflow and outflow. The thickness of each component is given.

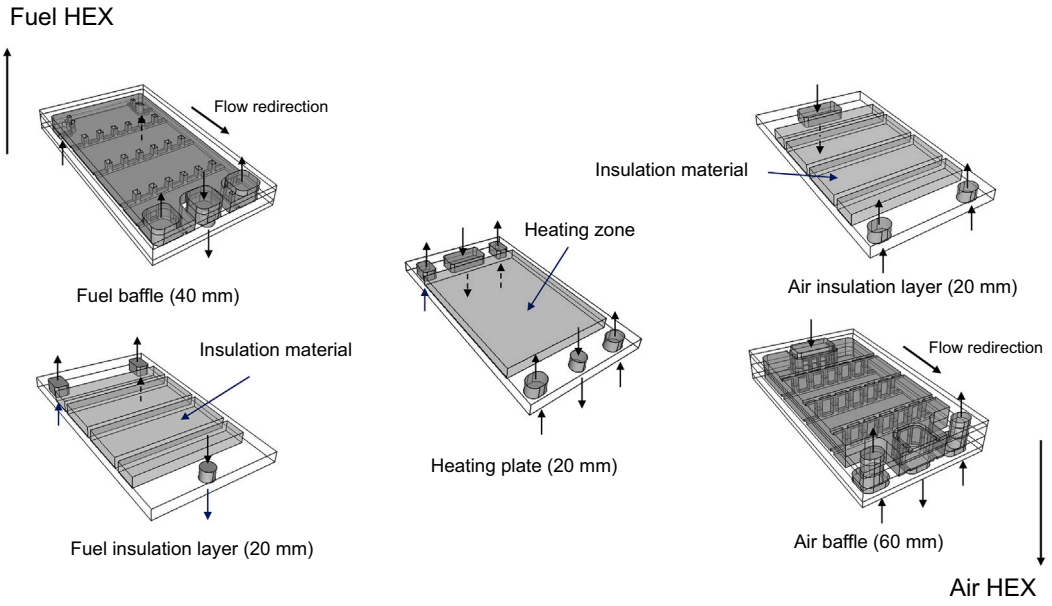

(b) Components in the IM remained as the original designs for the present numerical simulations. The thickness of each component is given.

Fig. 3. Components in the IM to be considered in the present study.

2.4. Numerical treatment

2.4.1. Geometry and meshing

The methodology proposed in the previous study [33] used a mesh generation technique that first created a 2-D surface mesh in the in-plane direction, then extruded it normally to the surface to achieve a prescribed thickness, as also shown by Fig. 2(b). While this method was effective for representing sub-stacks, applying it to an IM with various sub-components and diverse geometrical configurations presents significant meshing challenges. Recognizing that each component within the IM is physically separated by a finite space, in this study, an alternative meshing strategy was employed. The approach involves generating independent meshes for each sub-component, avoiding the complexities associated with creating a unified mesh across different geometries. The simplified geometries and corresponding meshes are generated using the open-source platform SALOME 9.9.

To facilitate field interpolations between different components within the manifolds, the AMI technique, introduced in OpenFOAM, is used. This method allows for various interpolation schemes; this study uses a surface area-weighted scheme. Preliminary results indicate that this interpolation method performs well, with negligible discrepancies observed between different mesh configurations. For other zones, particularly those where heat radiation and heat balance are critical, the authors propose using a 1-D model (introduced below). This simplified approach aims to address the computational challenges associated with these complex thermal phenomena while maintaining an acceptable level of accuracy.

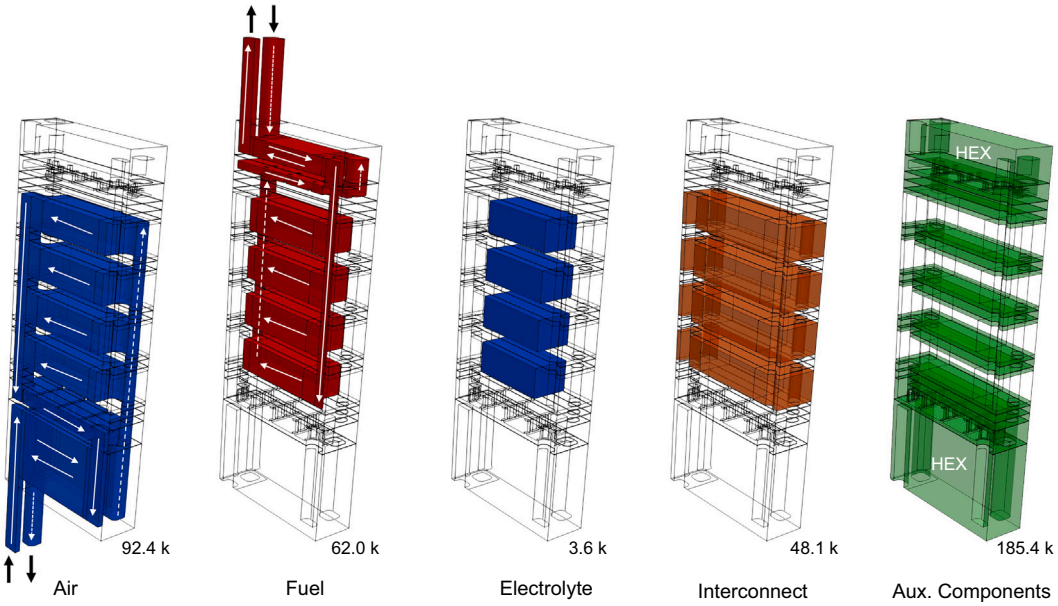

Fig. 4. The computational regions in the present study. The number of computational elements in each region is also shown. The total number of computational elements is 391,500.

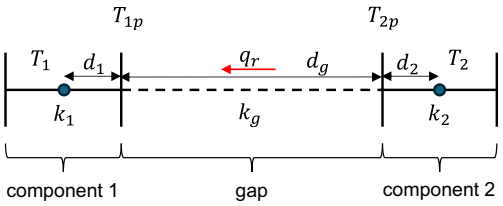

Fig. 5. A simple heat transfer description between components 1 and 2 through a gap.

2.4.2. 1-D thermal model

Thermal radiation is a critical factor in the operation of rSOC IMs and related systems [8]. The current design includes a 10 cm thick silica insulation layer around the IM, which effectively minimizes heat loss to the environment. Therefore, radiative heat losses to the surroundings are considered negligible for this model. The IM assembly has 1 mm thick gaps between all sub-components, with manifold zones separated by mica gaskets. Due to the high operating temperatures of SOC systems, radiative heat transfer is a very important mechanism of thermal energy transport between sub-components.

Traditional methods for modeling radiative heat transfer, such as the surface-to-surface approach and the discrete ordinates method, offer high accuracy but require significant computational resources. To optimize computational efficiency while maintaining model accuracy, the authors propose a pseudo-1-D radiative/conductive heat transfer model. This 1-D approximation captures the essential physics of radiative/conductive heat transfer, aiming to balance computational efficiency with model accuracy and providing a practical solution for analyzing thermal radiation in SOC IM systems. The 1-D model is proposed below.

The heat transfer through a gap between two components, labeled 1 and 2, can be simplified as shown in Fig. 5. The heat transfer is defined as a boundary condition for each side. In this scenario, the heat flux can be expressed as,

$$\frac{T_{1,\mathrm{p}}-T_1}{d_1}k_1=-\frac{T_{2,\mathrm{p}}-T_2}{d_2}k_2=\frac{T_{2,\mathrm{p}}-T_{1,\mathrm{p}}}{d_\mathrm{g}}k_\mathrm{g}+q_\mathrm{r} \tag{1}$$

where T is a localized temperature, d is the distance, k is thermal conductivity, q_r refers to the normal heat flux due to radiation, and the subscript p represents the values on the boundaries. This equation can be rearranged to obtain an expression for $T_{1,\mathrm{p}}$,

$$T_{1,\mathrm{p}}=\omega T_1+(1-\omega)T_\mathrm{ref} \tag{2}$$

with,

$$\omega=\frac{\frac{k_1}{d_1}}{\frac{k_1}{d_1}+\frac{k_\mathrm{g}}{d_\mathrm{g}}-\frac{q_\mathrm{r}}{T_{1,\mathrm{p}}}}, \tag{3}$$

$$T_\mathrm{ref}=\frac{\frac{k_\mathrm{g}}{d_\mathrm{g}}}{\frac{k_\mathrm{g}}{d_\mathrm{g}}-\frac{q_\mathrm{r}}{T_{1,\mathrm{p}}}}T_{2,\mathrm{p}} \tag{4}$$

The formulation corresponds to a 'mixed' boundary condition defined in OpenFOAM. The expression of $T_{2,\mathrm{p}}$ can be calculated similarly. A simplified form is employed here to describe the radiative heat transfer from component 2 to component 1 [40],

$$q_\mathrm{r}=\frac{\varepsilon}{2-\varepsilon}\sigma_\mathrm{B}(T_{2,\mathrm{p}}^4-T_{1,\mathrm{p}}^4) \tag{5}$$

where ε represents the emissivity of 'visible' surfaces, and σ_B is the Stefan-Boltzmann constant.

This simplified approach significantly reduces computational demands compared to more complex radiation methods. Additionally, this method addresses an issue in radiation modeling where mesh inconsistencies between adjacent surfaces can lead to non-conservative radiative heat flux q_r calculations, causing thermal imbalances. This study uses a radiation model along with the AMI interpolation algorithm. It is especially suitable for large-scale SOC system simulations, such as the present configuration, where radiative effects are present but can be sufficiently captured using a lower-dimensional model.

2.4.3. Region-to-region coupling

Given the numerous sub-components in the current IM, heat transfer becomes crucial and slows down the overall numerical calculations. The

solution to the conjugate heat transfer problem between fluid (air and fuel) and solid parts (interconnect and auxiliary components) can be numerically accelerated by using a surface coupling approach between different regions,

$$\begin{cases} [\boldsymbol{A}_\mathrm{f}][\boldsymbol{T}_\mathrm{f}] = [\boldsymbol{b}_\mathrm{f}] & \partial\Omega_\mathrm{f} \\ [\boldsymbol{A}_\mathrm{s}][\boldsymbol{T}_\mathrm{s}] = [\boldsymbol{b}_\mathrm{s}] & \partial\Omega_\mathrm{s} \end{cases} \Leftrightarrow \begin{bmatrix} \boldsymbol{A}_\mathrm{f} & \boldsymbol{B}_\mathrm{fs} \\ \boldsymbol{B}_\mathrm{sf} & \boldsymbol{A}_\mathrm{s} \end{bmatrix} \begin{bmatrix} \boldsymbol{T}_\mathrm{f} \\ \boldsymbol{T}_\mathrm{s} \end{bmatrix} = \begin{bmatrix} \boldsymbol{b}_\mathrm{f}^\mathrm{o} \\ \boldsymbol{b}_\mathrm{s}^\mathrm{o} \end{bmatrix} \partial\Omega_\mathrm{f} \cup \partial\Omega_\mathrm{s} \tag{6}$$

where $\boldsymbol{A}$ is a coefficient matrix, $\boldsymbol{T}$ represents the variables to be solved, $\boldsymbol{b}$ is the source term, and the subscripts, f and s, refer to fluid and solid domains, respectively. In the coupled matrix, the off-diagonal submatrices, $\boldsymbol{B}_{fs}$ and $\boldsymbol{B}_{sf}$, result from the heat transfer between different domains via their interfaces/boundaries.

In the DRA algorithm, a multiply-shared-space method is used. This means that some volumes may be shared by different components/parts. In this simulation, the electrolyte region is numerically shared by air, fuel, and interconnect, while the HEXs in the components region are numerically shared by air and fuel regions. Interphase heat transfers occur between these shared zones, described by the heat transfer equation in Table 1 as $\gamma \sum \alpha_\mathrm{j}(T - T_\mathrm{j})$. To address the temperature coupling issues, a region-to-region coupling approach introduced in a previous study [41] is used here. Assuming the indices i and j represent the physically shared points from two overlapping regions, and their meshes are compatible in the overlapping zones,

$$\begin{bmatrix} A_{11} & \cdots & A_{1i} & \cdots & 0 & \cdots & 0 \\ \vdots & \ddots & \vdots & \ddots & \vdots & \ddots & \vdots \\ A_{i1} & \cdots & A_{ii} + \alpha_{ij}^\mathrm{eff} & \cdots & -\alpha_{ij}^\mathrm{eff} & \cdots & 0 \\ \vdots & \ddots & \vdots & \ddots & \vdots & \ddots & \vdots \\ 0 & \cdots & -\alpha_{ji}^\mathrm{eff} & \cdots & A_{jj} + \alpha_{ji}^\mathrm{eff} & \cdots & A_{jm} \\ \vdots & \ddots & \vdots & \ddots & \vdots & \ddots & \vdots \\ 0 & \cdots & 0 & \cdots & A_{mj} & \cdots & A_{mm} \end{bmatrix} \begin{bmatrix} T_1 \\ \vdots \\ T_i \\ \vdots \\ T_j \\ \vdots \\ T_m \end{bmatrix} = \begin{bmatrix} b_1 \\ \vdots \\ b_i \\ \vdots \\ b_j \\ \vdots \\ b_m \end{bmatrix} \tag{7}$$

where the off-diagonal coefficients, α_{ij}^eff and α_{ji}^eff, arise from the interphase heat transfer coefficients. Typically, these inserted coefficients do not affect the symmetry of the original matrices. However, in cases with incompatible meshes, additional coefficients are introduced, resulting in an asymmetric coupling matrix. By using the surface and volume coupling approaches, the overall coupling matrix for temperature can be expressed as,

$$\begin{bmatrix} \boldsymbol{A}_\mathrm{a} & 0 & [\alpha_\mathrm{ae}] & \boldsymbol{A}_\mathrm{ai} & \boldsymbol{A}_\mathrm{ac} \\ 0 & \boldsymbol{A}_\mathrm{f} & [\alpha_\mathrm{fe}] & \boldsymbol{A}_\mathrm{fi} & \boldsymbol{A}_\mathrm{fc} \\ [\alpha_\mathrm{ea}] & [\alpha_\mathrm{ef}] & \boldsymbol{A}_\mathrm{e} & [\alpha_\mathrm{ei}] & 0 \\ \boldsymbol{A}_\mathrm{ia} & \boldsymbol{A}_\mathrm{if} & [\alpha_\mathrm{ie}] & \boldsymbol{A}_\mathrm{i} & \boldsymbol{B}_\mathrm{ic} \\ \boldsymbol{A}_\mathrm{ca} & \boldsymbol{A}_\mathrm{cf} & 0 & \boldsymbol{B}_\mathrm{ci} & \boldsymbol{A}_\mathrm{c} \end{bmatrix} \begin{bmatrix} \boldsymbol{T}_\mathrm{a} \\ \boldsymbol{T}_\mathrm{f} \\ \boldsymbol{T}_\mathrm{e} \\ \boldsymbol{T}_\mathrm{i} \\ \boldsymbol{T}_\mathrm{c} \end{bmatrix} = \begin{bmatrix} \boldsymbol{b}_\mathrm{a} \\ \boldsymbol{b}_\mathrm{f} \\ \boldsymbol{b}_\mathrm{e} \\ \boldsymbol{b}_\mathrm{i} \\ \boldsymbol{b}_\mathrm{c} \end{bmatrix} \tag{8}$$

where the diagonal submatrices, $\boldsymbol{A}$, represent the contributions from the energy transfer equation without the interphase heat transfer terms. The off-diagonal submatrices, $\boldsymbol{A}$, $\boldsymbol{B}$, and $[\alpha]$, represent the coupling coefficients from surface and volume coupling, surface coupling, and volume coupling, respectively. The subscripts a, f, e, i, and c denote the regions of air, fuel, electrolyte, interconnect, and components, respectively.

2.5. Implementation

The model includes all major physical processes within the IM, such as conjugate heat transfer, thermal radiation, and electrochemical reactions. The governing equations are discretized and solved in a finite domain using OpenFOAM-v2312, an open-source CFD library. Numerical simulations were performed on a computer with two AMD® EPYC™ 75F3 32-core CPUs. Calculations were run in parallel, using 3 cores. The average computational time for fuel cell operation simulations was less than 50 minutes per case, while electrolysis mode simulations took a maximum of 90 minutes per case.

3. Results

3.1. Model verification

The present model was first applied to simulate a smaller stack, referred to as F10, which has been studied in previous research [6,12,42,43]. This stack consists of 4 repeating units, each with an active area of 9 × 9 cm^2. Fig. 6 shows a schematic of this short stack, including supporting endplates on both the top and bottom. The stack was operated in an oven with a controlled environment. During operation, air and fuel (H_2) were supplied at rates of 2.13×10^{-4} kg/s and 2.16×10^{-5} kg/s, respectively, with the fuel humidified to 20 % water vapor content. The flows of air and fuel were in a counterflow pattern. The oven temperature was maintained at 700 °C, and the stack operated in fuel cell mode only for this experiment. Comparative simulations were conducted using both the present model and a detailed design model based on previous work [9,41]. To reduce computational resources, the detailed model considered only one repeating unit, while the present stack model was applied to the entire stack.

Fig. 6 compares the voltage-current curves. The numerical predictions from both models show good agreement with experimental measurements, with only minor deviations. The discrepancies between the two numerical methods are minimal across the entire range of load. While voltage-current curves provide insights into overall performance, local distributions are crucial for model accuracy. Therefore, reactant distributions across the flow regions were also compared in Fig. 6 between the two numerical methods. The mass fractions of oxygen and hydrogen decrease along the flow directions due to electrochemical reactions. Although the present model does not resolve the flow paths seen in the detailed model predictions, the overall distributions show excellent agreement. These results indicate that the present model accurately represents both the overall behavior of the stack and the local distributions of quantities, thereby validating its effectiveness for larger stack-level simulations.

3.2. Voltage-current relation of the integrated module

The system operates in dual modes, functioning as both a fuel cell and as an electrolyzer. During operation, various sub-components must work together to ensure optimal performance. A PID controller was used to regulate the air flow and the heating plate provides power. As a result, the operational parameters change in response to different current loads and modes. For this investigation, the operating conditions and physical parameters were standardized based on current density loads of 0.5 A cm^{-2} for fuel cell operation and −0.5 A cm^{-2} for electrolysis operation. The specific values for these parameters are listed, respectively in Tables 2 and 3. The uncertainties associated with the experimental measurements are summarized in the footnote and apply to all subsequent experimental results.[1] For a more detailed description of the experimental setup and procedures, we refer readers to our previous publications [10,11,13,14].

Fig. 7 shows the comparison between experimental results and numerical predictions. The operating parameters were set based on current density loads of 0.5 A cm^{-2}, excluding scenarios with much lower current densities. The data show good agreement between predicted and observed stack voltages at these current loads. For the input parameters given in Table 2, electrolysis mode exhibits higher temperatures at lower current loads, whereas fuel cell mode experiences lower temperatures at lower current densities, compared to the real operating conditions. Since area-specific resistance is inversely related to temperature, resistance is

[1] **Accuracy of thermocouples:** Type N thermocouples, Class 2 according to IEC 60584–1, operating in the temperature range of 40–1200 °C, have a deviation of ±2.5 °C or ±0.75 % (whichever is greater). **Accuracy of flow controllers/meters:** MFCs and MFMs: ±0.5 % of actual value plus ±0.1 % of full scale. Coriolis controllers (for deionized water): ±0.2 % of actual value plus ±0.2 g/h.

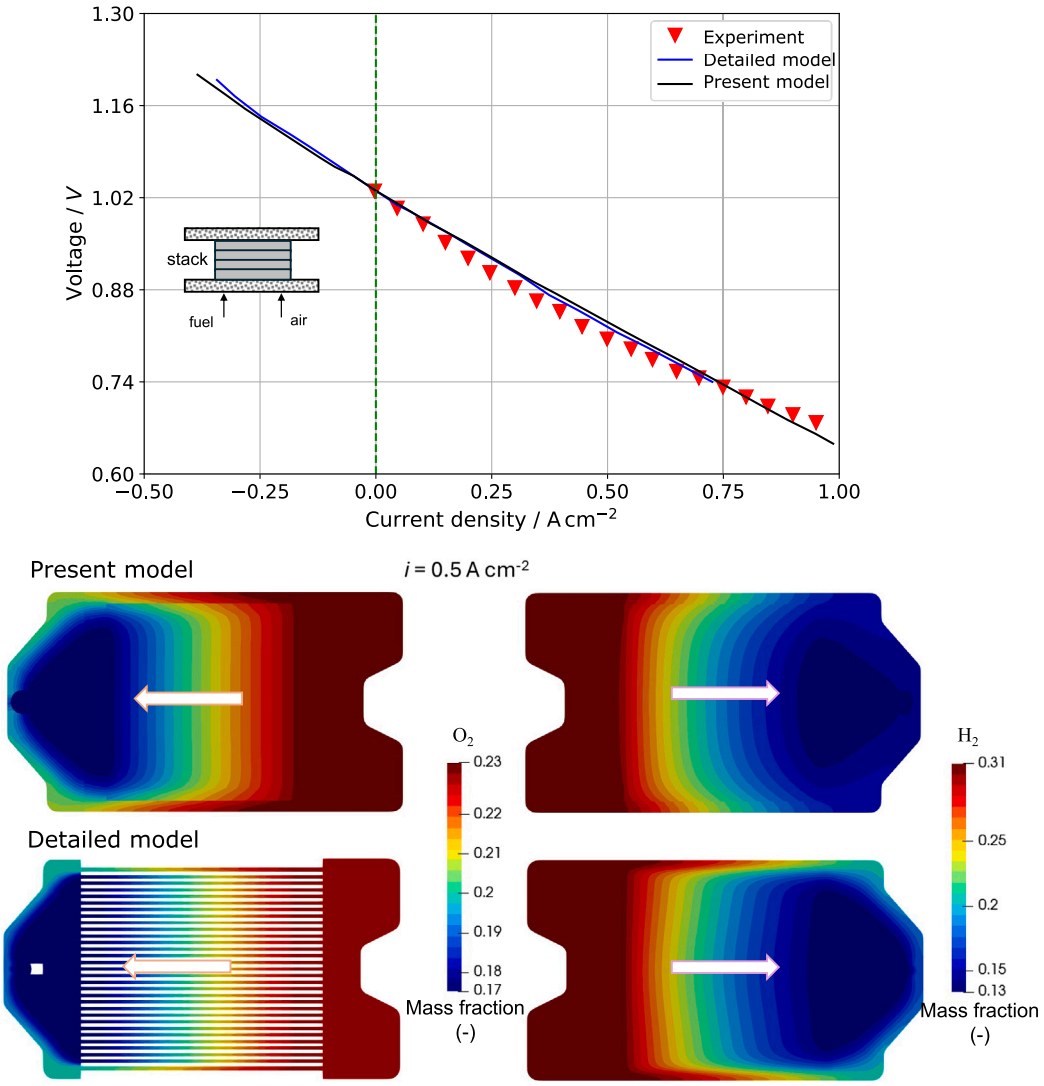

Fig. 6. Comparison between numerical results and experimental data for F10 stack design. Top: voltage-current relations of the detailed method, the present model, and the experimental results. Bottom: the mass fraction distributions of oxygen and hydrogen when the current density is 0.5 A cm^{-2}.

lower in electrolysis mode and higher in fuel cell mode. Therefore, stack voltages in both modes should be higher at lower current loads. It should be noted that these conditions do not represent actual stack operating parameters.

3.3. Fuel cell operation

In fuel cell operations, the HPLs are turned off due to the exothermic nature of the electrochemical reaction. Effective thermal management is essential to prevent the system from overheating. This is achieved by supplying sufficient ambient air, which acts as a coolant.

The air and fuel HEXs are crucial for the IM. These components should ensure efficient heat transfer from the hot exhaust outflow to the cold feedstock, thereby improving the overall efficiency. Fig. 8 compares numerical predictions and experimental measurements of temperatures at the middle of the HEXs. The results show very good agreement, with maximum temperature deviations of less than 15 K. Notably, the fuel side shows higher temperatures compared to the air side, due to the much lower fuel flow rate. A temperature increase is observed along the cold flow inlet directions, consistent with the heat transfer mechanism between the cold and hot fluids. The temperature profile on the air side is nearly linear, where the temperature distribution is predominantly governed by the high-velocity airflow and the larger thickness of the air-side HEX. In contrast, on the fuel side, the temperature rise is initially steeper but tends to flatten near the outlet. Given that the flow within these mini-channels remains laminar and the Prandtl numbers of both air and fuel are around 1, the thermal entrance length remains relatively short compared to the overall channel length. Therefore, fully developed thermal conditions dominate most of the flow region. The heat transfer characteristics between the solid walls and the fluid are described using the Nusselt number, which depends on the cross-sectional geometry of the channels. As a result, the heat transfer coefficients remain nearly uniform along the channel length. On the air side, the presence of an excess air supply ensures that the heat capacity rates of the inflow and outflow remain approximately equal. This leads to a relatively constant temperature difference between fluids and solids across the HEX and results in the observed linear temperature profile. On the fuel side, however, the heat capacity rate of the outflow is higher than that of the inflow. Hence, the solid temperature exhibits a steeper increase near the cold inlet and a more gradual rise toward the outlet. This effect is further amplified by the influence of the adjacent fuel baffle, whose temperature is higher at the fuel inlet side, thereby enhancing heat transfer in this region.

Table 2
Operating conditions.

Operations		Fuel cell	Electrolysis	Units
Pressure	Air	1.0	1.0	bar
	Fuel	1.0	1.0	
Temperature	Air	289	379	K
	Fuel	311	516	
Inlet	Air	750	77	NL min^{-1} *
	Fuel	188.6 (H_2)	14.2 (H_2) | 127.5 (H_2O)	
Heating power	HPL1	0	880	W"
	HPL2	0	943	
	HPL3	0	816	
	HPL4	0	807	
	HPL5	0	957	
Heat loss	Top	480	0	W°
	Side	716	780	
	Bottom	328	0	

* Normal liter per minute
" Power obtained from the control system
° Constant heat flux prescribed

Table 3
Physical parameters.

Description	Value	Units
Thickness (RPU)	0.004	m
Thermal conductivity (steel)	20*	W m^{-1} K^{-1}
Thermal conductivity (mica)	0.35	W m^{-1} K^{-1}
Radiative emissivity	0.816"	–
ASR (fuel cell)	$9.75\times10^{-9}\exp\left(-\frac{62715}{RT}\right)$	Ω m^2
ASR (Electrolysis)	$6.9\times10^{-9}\exp\left(-\frac{69005}{RT}\right)$	Ω m^2

* Mean value considering possible thermal resistance
" Constant value over all radiative surfaces

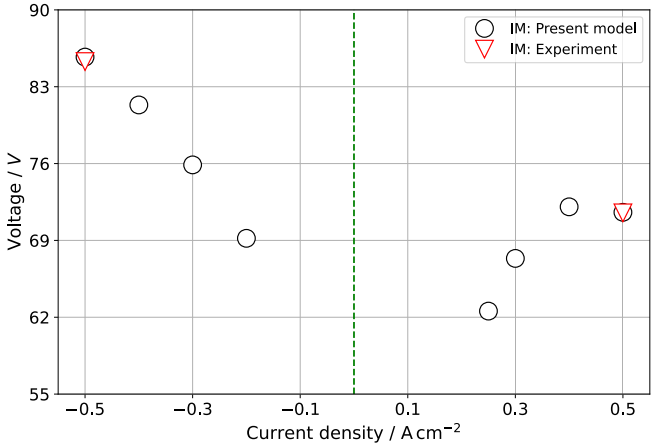

Fig. 7. Relationship between current density and stack voltage for the IM. The IM generally operates at a current load of 0.5 A cm^{-2}. Other data points were obtained under identical operating conditions and physical parameters for both fuel cell and electrolysis operations at the current load of 0.5 A cm^{-2}.

Fig. 9 compares temperatures across each sub-stack. The overall temperature distributions from inlet to outlet align well with experimental data. The central sub-stacks (numbers 2 and 3) show slightly higher temperatures compared to the peripheral sub-stacks (numbers 1 and 4) located at the bottom and top, respectively. A temperature increase is observed from the air/fuel inlet to the outlet, consistent with the exothermic nature of the electrochemical reaction. Temperature profiles at the center of the sub-stacks reveal substantially higher temperatures compared to the boundaries, due to heat transfer from the side

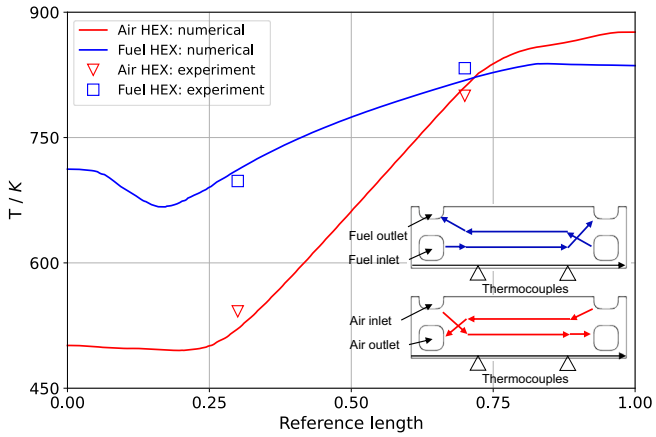

Fig. 8. Comparison of temperature profiles at air/fuel HEXs in the IM, i = 0.5 A cm^{-2}. The positions of related thermocouples are marked. The numerical results are plotted along the line shown in the sketch.

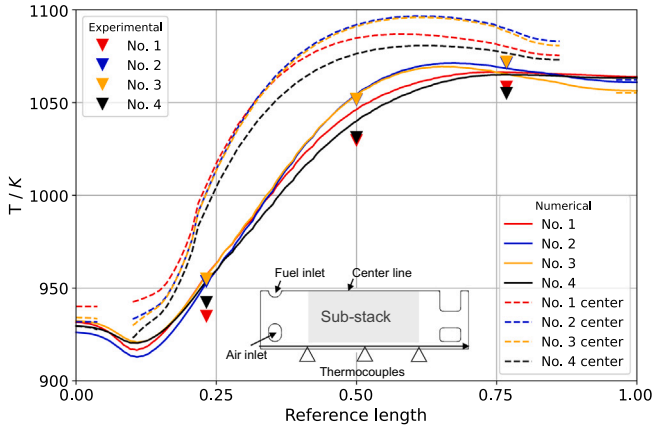

Fig. 9. Comparison of temperature profiles at 4 × sub-stacks in the IM, i = 0.5 A cm^{-2}. The positions of related thermocouples are marked. The numerical results are plotted over the line shown in the sketch. The stacks are labeled starting from the bottom (air) to the top (fuel) sides.

wall surfaces. The temperature rise is more pronounced near the inlet zones and gradually slows down toward the outlet. This is attributed to the higher local current density near the inlets, due to higher reactant concentrations. As a result, the heat generation rate is greater in this zone, leading to a more rapid temperature increase. The slight temperature reduction observed is due to heat losses through the boundaries. Additionally, it is notable that the temperatures within the central zones of the stacks are 40–50 K higher than those recorded by the thermocouple measurements.

The close match between predicted and measured temperature profiles in both the HEXs and sub-stacks validates the accuracy of the present solution method. This computational approach demonstrates high fidelity in predicting 3-D temperature distributions across the IM, providing a valuable tool for further analysis in SOC systems.

The temperature distributions predicted by the current numerical model are shown in Fig. 10. The cold air and fuel streams are heated as they pass through the HEXs, using the thermal energy from the hot exhaust gases. It is important to note that the air and fuel HEX zones allow both incoming and outgoing flows. The temperature profiles are displayed separately for inflow and outflow. The small temperature differences between the incoming and outgoing flows for both air and fuel sides indicate high thermal efficiency. As the air and fuel move through the sub-stacks, their temperatures rise due to the exothermic nature of

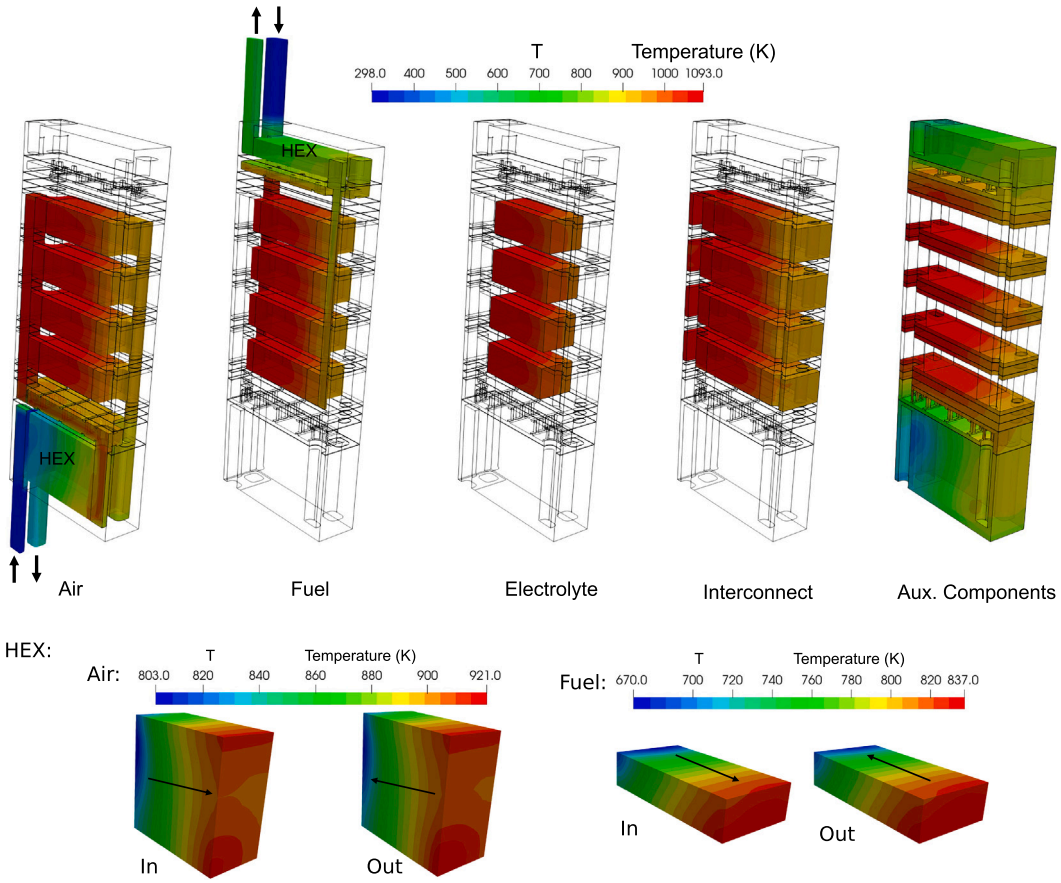

Fig. 10. Temperature distributions in each component of the IM, $i = 0.5$ A cm^{-2}. The comparisons of inflow and outflow temperature distributions are shown at the bottom.

the electrochemical reactions. Additionally, it is observed that when the heated air passes through the air baffle zones, the flow near the walls cools down, while the central flow remains hot. This can be attributed to the relatively high air flow rate.

Further examination of the solid components within the sub-stacks, specifically the electrolyte and interconnect, reveals that these elements have the highest temperatures compared to other components, with peak temperatures in their central regions. The temperature distributions across the various components in the components region show finite discontinuities, due to the predominance of radiative heat transfer between them. The HPLs are at temperatures slightly lower than the interconnects, due to thermal losses from the side wall surfaces. Lower temperatures are observed in components farther from the stacks, such as the air/fuel baffle zones and air/fuel HEXs. This is due to the influence of insulation layers, cold air/fuel inlets, and radiative heat transfer from hot to cold objects. The presence of insulation layers on both sides helps reduce heat losses, maintaining very similar temperature distributions between sub-stacks.

Fig. 11 shows the distributions of additional parameters. The electrochemical reactions result in the consumption of reactants (oxygen and hydrogen) and the production of water on the fuel side. As the reactants flow through the reaction zones, their molar fractions decrease. This reduction in reactant concentration leads to a corresponding decrease in current densities, as the Nernst potential decreases. It is noteworthy that the current density distributions across each sub-stack are very similar. The volume-averaged distribution of the stack voltage is also presented, which corresponds to the overall voltage output from the IM. The spatial distributions of temperature, reactant concentration, current density, and stack voltage provide important data for elucidating the performance and durability of the stack/IM. A uniform distribution of current density across sub-stacks has the potential to mitigate the formation of localized thermal gradients, thereby reducing thermal stresses and contributing to the prolonged longevity of stack components. Furthermore, the gradual depletion of reactants along the flow direction promotes efficient reactant utilization, minimizing the risks of concentration polarization and fuel starvation—phenomena that could otherwise impair operational efficacy. Collectively, these attributes may enhance overall stack efficiency, extend the operational lifespan of the system, and support the scalability of stack designs for applications requiring larger configurations.

3.4. Electrolysis operation

In electrolysis operations, the HPLs are activated due to the endothermic nature of the electrochemical reaction when the cell voltage falls below the thermal neutral voltage. These HPLs, strategically placed around the sub-stacks, help maintain reasonable stack temperatures, reducing ohmic and activation overpotential losses. The system uses an external steam generator to produce the water vapor necessary for electrolysis. Unlike in fuel cell mode, the airflow is significantly reduced, as its main function shifts from temperature regulation to oxygen removal. Although both air and fuel inlets are preheated, inlet temperatures are relatively low compared to operating conditions. Nevertheless, the HEXs continue to play a crucial role in raising inlet flow temperatures and improving overall system efficiency in the current rSOC IM design.

Fig. 12 presents a comparative analysis of numerically predicted temperature profiles and experimental measurements from thermocouples. The differences between numerical and experimental results are smaller in magnitude compared to fuel cell operations, due to the lower airflow rate. The fuel HEX shows lower temperatures than to the air HEX, due

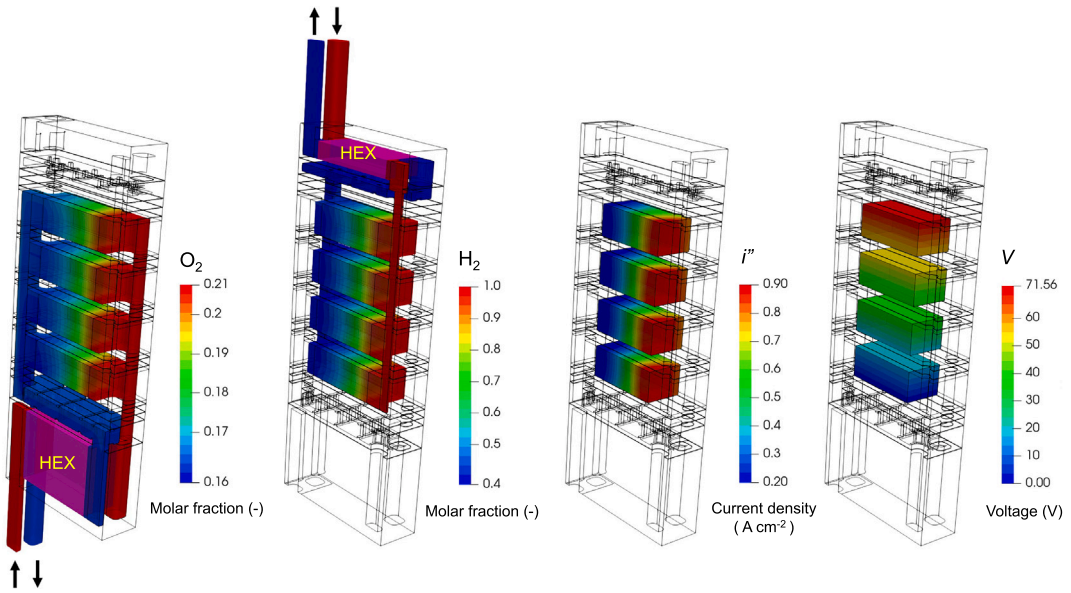

Fig. 11. Distributions of oxygen and hydrogen molar fractions, current density, and stack voltage, in the IM, $i = 0.5$ A cm^{-2}. The colors in the HEX zones are mixtures of maximum and minimum. The voltage variation in each cell is minimal (within 10 mV), with slightly higher values observed in the middle layers.

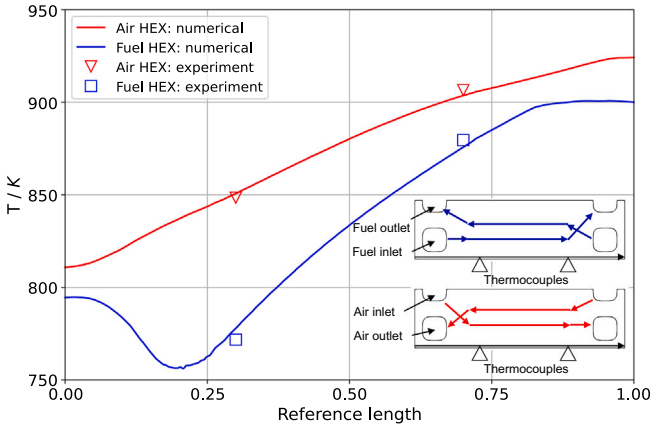

Fig. 12. Comparison of temperature profiles at air/fuel HEXs in the IM, $i = -0.5$ A cm^{-2}. The positions of related thermocouples are marked. The numerical results are plotted over the line shown in the sketch.

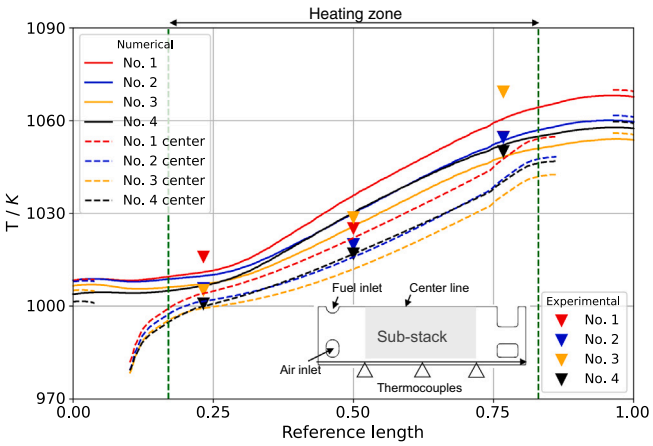

Fig. 13. Comparison of temperature profiles at 4 × sub-stacks in the IM, $i = -0.5$ A cm^{-2}. The positions of related thermocouples are marked. The numerical results are plotted over the line shown in the sketch. The rightmost point of sub-stack 3 from experimental results is due to minor leakage and possible hydrogen burning. The sub-stacks are labeled starting from the bottom (air) to the top (fuel) sides.

to the higher fuel inflow rate and heat capacity from increased steam content, in addition to lower inlet temperature. It is observed that the temperature profiles in the middle zones of both the air and fuel HEXs are similar to those observed during fuel cell operation. On the air side, the heat capacity rate at the outflow exceeds that at the inflow, leading to a slightly steeper temperature gradient near the cold inlet. Conversely, on the fuel side, the outflow heat capacity rate is lower than that at the inlet, suggesting a flatter temperature gradient near the cold inlet. However, due to the smaller thickness of the fuel HEX, its temperature profile is largely influenced by the adjacent fuel baffle, particularly given the high temperature at the inlet side, which influences the expected gradient.

The temperature distribution within the sub-stacks is crucial for accurately estimating temperature profiles and characterizing stack performance. Fig. 13 shows the temperature profiles predicted by the current numerical methods alongside experimental measurements. The heating zones are marked by dashed green lines. A temperature increase is observed from the inlet to the outlet due to heat generated by the HPLs. Compared to fuel cell mode, the temperature variation from inlet to outlet is more uniform, reducing thermal gradient-induced stress. This active thermal control strategy helps minimize temperature non-uniformity. Maximum deviations between numerical and experimental results are observed in the central zones, possibly due to radiative transfer from the HPLs, and/or limitations in the simplified radiation model. Temperature profiles at the stack center show lower temperatures, consistent with the endothermic nature of the electrochemical reaction. Given the assumption of uniform heat generation from the HPLs across the heating zones, the temperature profiles are expected to exhibit a rather linear trend from the inlets to the outlets. However, owing to the endothermic electrochemical processes, the temperature gradients are observed to be less pronounced near the inlet regions. Concurrently, thermocouple measurements indicate temperatures that are 10–20 K higher than those at the stack centers. A significantly high temperature was observed at the rightmost thermocouple of sub-stack

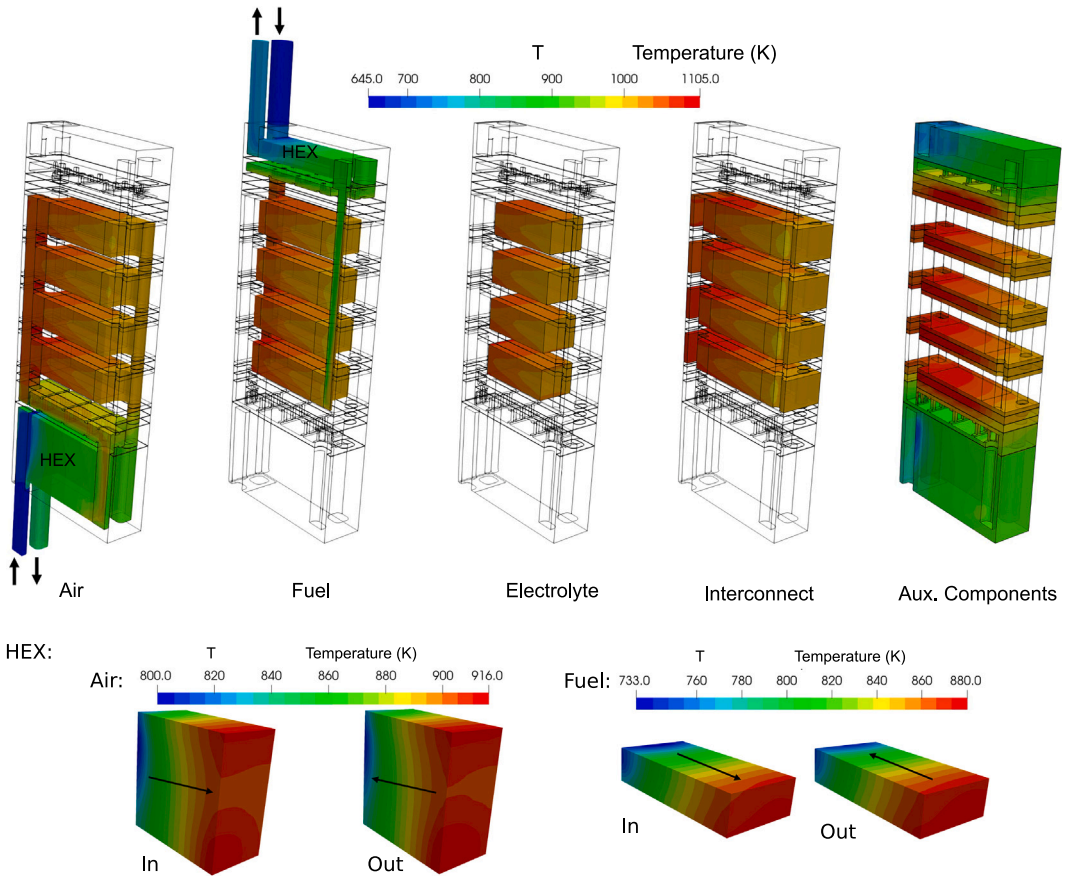

Fig. 14. Temperature distributions in each component of the IM, $i = -0.5$ A cm^{-2}. The comparisons of inflow and outflow temperature distributions are shown at the bottom.

3. This area has a minor leakage between the fuel and air sides, causing some hydrogen to burn locally near it, resulting in higher local temperatures.

Fig. 14 shows the temperature distributions across various regions of the system. The cold air and fuel/steam mixture enter the IM and are heated in the HEXs. Due to the higher fuel/steam inflow rate, the fuel-side HEX has lower temperatures, while the air-side HEX, with its lower inflow rate, has higher temperatures. As the air and fuel/steam mixture move through the stack zones, they are heated by the interconnects, which conduct heat radiated from the HPLs. Within the air baffle zone, a slight temperature difference is observed, with the air near the walls being slightly cooler than the bulk flow. The relatively minor temperature differences between the inlet and outlet flow for both air and fuel/steam sides indicate high HEX efficiency.

Examination of the sub-stacks reveals lower temperatures in the central regions, as shown in the electrolyte and interconnect areas. The electrolyte region has slightly lower temperatures across the domain due to endothermic electrochemical reactions. Notably, the temperature profiles across sub-stacks are similar, as also shown in Fig. 13. Among the various components, the HPLs have the highest temperatures. The insulation layers on both air and fuel/steam sides effectively reduce heat losses to adjacent baffle zones. This results in much lower temperatures in the baffle zones compared to the neighboring insulation layers. In the HEXs, the fuel/steam side shows more pronounced cooling effects from the inflow.

Fig. 15 shows the distributions of several additional relevant parameters. The products, oxygen, and hydrogen, become increasingly concentrated as the air and fuel flows pass the sub-stacks due to ongoing electrochemical reactions. The current density decreases along the flow direction in the co-flow region, due to the increasing concentration of products and decreasing concentration of reactant (water), which results in higher Nernst potentials. The current density distributions are very similar among the sub-stacks. The stack voltage distribution is also displayed, indicating that the cell voltages are relatively uniform. Consistent with fuel cell operation, these detailed spatial distributions effect inform the optimization of stack and IM designs, thereby improving overall stack efficiency, prolonging the operational lifespan, and facilitating the scalability of stack configurations for applications necessitating larger-scale implementations.

In electrolysis operations, the power of each HPL is controlled by the PID controller. Thermocouples, placed at key points within each HPL as shown in Fig. 16, provide temperature feedback. The controller adjusts the heating power to keep the temperature at 825 ^{o}C. For comparison, numerical predictions are also shown. Within the middle of the heating zones, the temperatures of HPLs 2, 3, and 4 exhibit an increase consistent with the temperature profiles observed in the sub-stacks. At the inlet and outlet zones, temperatures are comparatively lower due to the presence of gaskets. HPLs 1 and 5, positioned at the lowermost and uppermost of the sub-stacks, are adjacent to insulation layers that conduct more heat via the gaskets. Therefore, the maximum temperatures in these HPLs are displaced near the middle of the heating zones. The simulation results indicate that the predicted temperatures at certain points are slightly lower than the target temperature, with the largest difference being about 15 K in the top and bottom HPLs (units 1 and 5). While these discrepancies are within an acceptable range given the complexity of the system, they underscore potential challenges in relying solely on model-calibrated control systems for real-world applications without additional refinement.

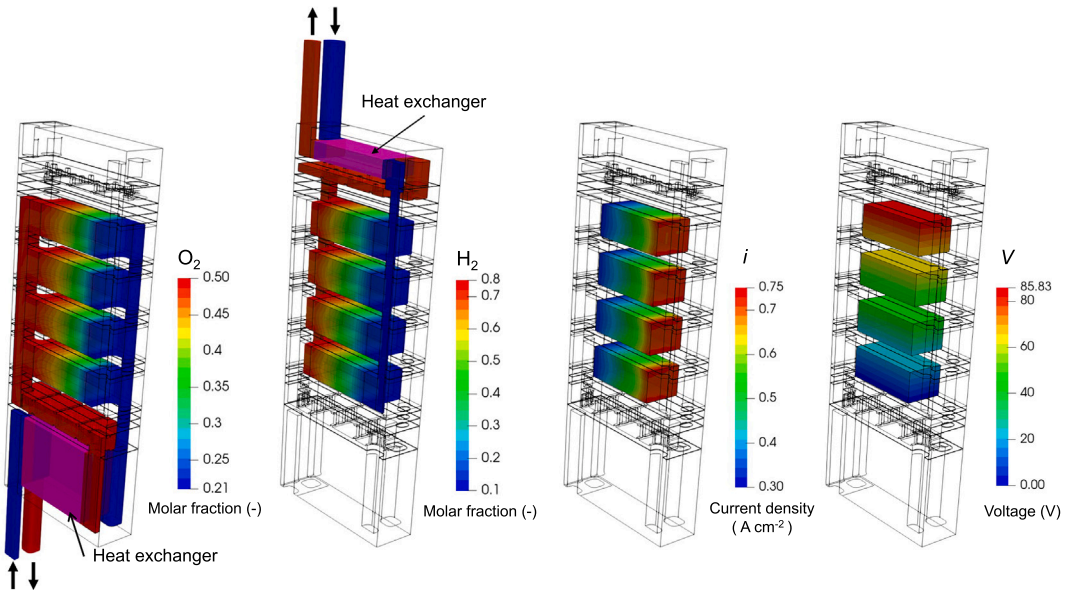

Fig. 15. Distributions of oxygen and hydrogen molar fractions, current density, and cell voltage, in the IM, $i = -0.5$ A cm^{-2}. The colors in the HEX zones are mixtures of maximum and minimum.

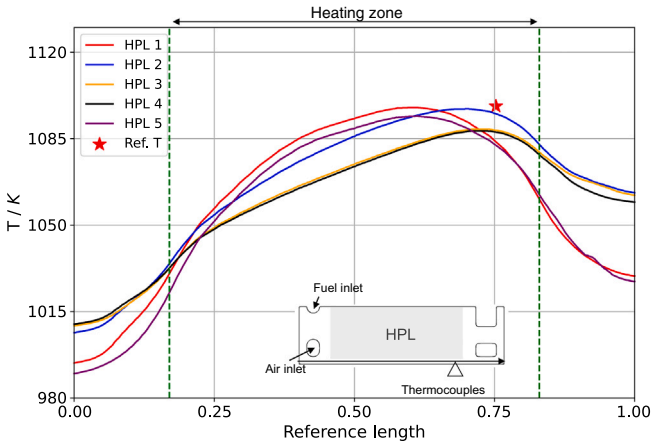

Fig. 16. Comparison between numerical results and experimental data for the HPLs in IM. The positions of related thermocouples are marked. The numerical results are plotted over the line shown in the sketch. The HPLs are labeled starting from the bottom (air) to the top (fuel) sides.

4. Discussion

The numerical methods proposed in this study are able to accurately predict temperature profiles that agree well with experimental measurements. While minor deviations exist, they are acceptable given the complexity of the IM. The present model facilitates informed design optimization by providing detailed 3-D insights into local temperature distributions, species concentrations, and current densities, information that extends beyond the scope of experimental measurements alone. Temperature profiles enable accurate predictions of thermal behavior and provide a basis for minimizing temperature variations while enhancing overall temperature uniformity over the repeating units and stacks. Species distributions are critical for material behavior, for example, stability under oxidizing conditions [44], as well as assessing reactant uniformity and the risk of starvation. In addition, the current density distribution is a key parameter of the stack and system performance. A more uniform current density within individual repeating units correlates with improved cell-level efficiency, while consistent distributions across repeating units and sub-stacks signify good stack design. Beyond these factors, pressure losses and heat dissipation are also pivotal in stack design. Although various criteria influence the optimization of cells, stacks, and systems, the objectives typically center on maximizing power density, enhancing overall efficiency [10], and ensuring long-term operational stability [45,46]. The present model could contribute to reducing total system costs, aligning practical engineering and economic goals [47].

An important assumption in this study is the uniform distribution of heat losses over IM surfaces, which, given the complex thermal behavior involved, may represent an oversimplification. The current IM design incorporates a 10 cm thick insulation material intended to minimize heat losses to the ambient environment. Residual heat dissipation persists and is influenced by insulation properties, thermal conductivity, and local temperature gradients. Although radiative heat loss is expected to be minimal, accurately quantifying heat loss rates remains challenging due to spatial variations. Future research should address this limitation by integrating a more sophisticated model incorporating spatially variable heat transfer coefficients, thereby improving the accuracy of thermal predictions for the IM.

This study neglects the internal participative radiative heat transfer while accounting for the external surface-to-surface radiative heat transfer between sub-components within the IM. For internal radiation, previous studies have shown mixed results regarding the importance of internal radiative heat transfer. Some researchers [48,49] have found these effects to be minor, while others [50,51] have indicated that surface-to-surface radiation between internal boundaries may be significant. A previous work by the present authors [33] examined radiative heat transfer in channels and found it to be minimal. However, the effects in manifolds and transition zones are still unclear and need further study. When it comes to surface radiation, the adoption of a simplified 1-D model mitigates the computational burden associated with simulating radiative heat transfer between sub-components, such as between the outer surfaces of sub-stacks and HPLs. This simplification assumes uniform emissivity across all surfaces and disregards the influence of surrounding areas, potentially oversimplifying the radiative environment. In reality, surface radiation is likely more heterogeneous, varying with spectral properties, temperature gradients, and view factors, which the pseudo-1-D approach does not capture. The observed deviations, particularly the temperature discrepancies in the electrolysis mode, may partly

result from these simplifications. It is suggested that radiative contributions, both internal and external, could affect the accuracy of predicted thermo-fluid conditions. These limitations highlight the need for a more comprehensive radiation model in future work, potentially integrating multi-dimensional radiation effects and variable emissivity to refine the representation of heat transfer within the IM.

While the numerical model of the IM exhibits good agreement with experimental data under reference conditions, its reliance on several simplifying assumptions underscores the need for a comprehensive sensitivity analysis to assess its predictive robustness. Such an analysis would systematically vary key parameters, including radiative emissivities, inlet temperatures, air and fuel/steam flow rates, and HPL power in electrolysis mode, to evaluate their impact on simulated behavior, such as temperature distributions, species concentrations, and current densities. Quantifying the extent to which these parameters contribute to observed discrepancies will help distinguish deviations arising from model assumptions from those due to operational variability. In addition, sensitivity analysis offers valuable insights for optimizing design and operational strategies, enabling improvements in sub-stack uniformity, mitigation of overheating, and prevention of reactant starvation, thereby enhancing overall system reliability under diverse operating conditions. The present study prioritizes model validation by establishing a baseline through detailed comparison with experimental data, laying the groundwork for subsequent investigations into parametric effects and system refinements. Given the large number of influential parameters involved, a dedicated follow-up study is essential to systematically explore their interactions and impacts, thereby ensuring the applicability of the present model to real-world stack/system performance optimization.

The simplified conduction-radiation formulation, Eqs. (1)-(4), was chosen as a balance between accuracy and speed. A detailed surface-to-surface formulation would require radiation view factors to be computed [40], adding substantial resource requirements to the calculation procedure. At the same time, completely ignoring radiative transfer (as so many authors do) is inaccurate, since it is the primary mode of heat transfer in the gap region between the individual cells, separated by the manifold gaskets. Since the gap separating the cells is small (1 mm), the incident subtended solid angles will be regionally localized, and it is therefore reasonable to presume planar geometry based on a single pair of opposing temperature values. It is to be noted that even though the gap is small, it is large compared to molecular scales, so that 'far field' (not 'near field') radiation theory will apply. A matter of concern, however, is the choice of emissivity, ϵ, and the presumption that the surfaces may be treated as diffuse grey, i.e., neglecting directional and wavelength effects. Studies indicate that the hemispherical emissivities of stainless steel are in the range 0.075 to 0.85: the choice of this value will clearly impact the temperature distribution, and further research is clearly required.

Another critical aspect of real-world IM and system operation is transient behavior, consisting of start-up, shut-down, load fluctuations, and transitions between fuel cell and electrolysis modes. These dynamic conditions lead to transient responses in thermal and electrochemical processes, among others, which steady-state simulations cannot fully capture, thereby limiting the accuracy of performance predictions. For instance, rapid heating during start-up or mode switching can generate large temperature gradients, increasing the risk of thermal-mechanical failure in the cell and stack. Similarly, load variations may lead to uneven current distributions, accelerating material degradation and performance deterioration. Integrating transient analysis into the modeling framework can facilitate the development of robust operating and advanced control strategies to dynamically adjust system parameters, maintain optimal temperatures, and mitigate inefficiencies or structural damage. Future studies will incorporate time-dependent simulations, integrating the current model with transient gas flow and heat transfer dynamics to enhance predictive capabilities and operational reliability.

5. Conclusions

This study successfully developed a multiscale and multiphysical numerical modeling approach using OpenFOAM to analyze the performance of a 10/40 kW rSOC IM designed at Forschungszentrum Jülich GmbH. By incorporating key numerical techniques, such as the AMI for sub-component interpolation, a 1D radiative heat transfer model for inter-component heat exchange, and a region-to-region coupling approach for thermal interactions, the model provides a comprehensive and computationally efficient framework for IM-level analysis.

A comparison between the present model and a detailed model applied to a smaller F10 stack demonstrates the fidelity of the current approach. Validation against experimental data on the IM demonstrated good agreement in both fuel cell and electrolysis modes, with maximum temperature deviations of 10 K – 15 K in the middle parts of sub-stacks. The model effectively captured the temperature uniformity of sub-stacks and the high efficiency of the integrated HEXs. Furthermore, the analysis of species and current density distributions supports the fact that IM design is able to ensure consistent performance of sub-stacks, a critical factor for long-term system reliability.

The simulation results offer a complete insight into the IM during operation, which enables a much more detailed understanding of local temperatures, concentrations, and current densities than is possible with the present generation of experimental methods. With this, the present model can be used as an effective tool for the development of future system designs as well as operating strategies for highly sophisticated rSOC systems.

Future investigations will expand the capabilities of the present model by addressing critical limitations and broadening its predictive scope across multiple dimensions: 1) refining the radiation model to more accurately represent thermal radiative heat transfer processes within the IM; 2) performing a comprehensive sensitivity analysis to assess the impact of operational parameters on thermo-fluid and electrochemical performance, thereby quantifying their contributions and informing design optimization strategies for improved stack/system efficiency; 3) deriving meaningful design parameters for stack/IM and/or operational strategies, with the aim of optimizing module performance; 4) conducting transient studies to simulate dynamic operations, such as start-up, shut-down, load variations, and transitions between fuel cell and electrolysis modes; and 5) developing models to characterize long-term degradation phenomena, thereby improving the understanding of the performance and durability of SOC stacks/systems.

CRediT authorship contribution statement

Shidong Zhang: Writing – review & editing, Writing – original draft, Validation, Software, Methodology, Investigation, Data curation, Conceptualization. **Roland Peters:** Writing – review & editing, Supervision, Resources, Funding acquisition, Data curation. **Nicolas Kruse:** Writing – review & editing, Validation, Data curation. **Robert Deja:** Validation, Data curation. **Steven B. Beale:** Writing – review & editing, Writing – original draft, Supervision, Methodology, Formal analysis. **Remzi Can Samsun:** Writing – review & editing, Writing – original draft, Resources, Project administration. **Rüdiger-A. Eichel:** Writing – review & editing, Resources, Funding acquisition.

Declaration of competing interest

The authors declare the following financial interests/personal relationships which may be considered potential competing interests:

Ruediger-A Eichel reports that financial support was provided by Federal Ministry of Education and Research Berlin Office. Reports a relationship with that includes: Has patent pending to. If there are other authors, they declare that they have no known competing financial interests or personal relationships that could have appeared to influence the work reported in this paper.

Acknowledgement

The authors extend their gratitude to the colleagues at Forschungszentrum Jülich GmbH for their invaluable support, particularly Messrs Shangzhe Yu, Wilfried Tiedemann, and Rabah Lekehal. We also gratefully acknowledge the financial support from the Helmholtz Society, the German Federal Ministry of Education and Research, and the Ministry of Culture and Science of the Federal State of North Rhine-Westphalia.

Appendix A. Supplementary data

Supplementary data for this article can be found online at doi:10.1016/j.apenergy.2025.126626.

Data availability

Data will be made available upon request.

References

[1] Global Hydrogen review 2023 – analysis. https://www.iea.org/reports/global-hydrogen-review-2023
[2] World Energy outlook 2023 – analysis. https://www.iea.org/reports/world-energy-outlook-2023
[3] Mogensen MB, Chen M, Frandsen HL, Graves C, Hansen JB, Hansen KV, et al. Reversible solid-oxide cells for clean and sustainable energy. Clean Energy 2019;3(3):175–201. https://doi.org/10.1093/ce/zkz023
[4] Gür TM. Review of electrical energy storage technologies, materials and systems: challenges and prospects for large-scale grid storage. Energy Environ Sci 2018;11(10):2696–767. https://doi.org/10.1039/C8EE01419A
[5] Wolf SE, Winterhalder FE, Vibhu V, de Haart LGJB, Guillon O, Eichel R-A, et al. Solid oxide electrolysis cells – current material development and industrial application. J Mater Chem A 2023;11(34):17977–8028. https://doi.org/10.1039/D3TA02161K
[6] Fang Q, Blum L, Peters R, Peksen M, Batfalsky P, Stolten D. SOFC stack performance under high fuel utilization. Int J Hydrogen Energy 2015;40(2):1128–36. https://doi.org/10.1016/j.ijhydene.2014.11.094.
[7] Nemati A, Rizvandi OB, Nakashima RN, Beyrami J, Frandsen HL. Multiscale multiphysics modeling of ammonia-fueled solid oxide fuel cell: effects of temperature and pre-cracking on reliability and performance of stack and system. Appl Energy 2024;373:123913. https://doi.org/10.1016/j.apenergy.2024.123913
[8] Beale S, Andersson M, Boigues-Muñoz C, Frandsen HL, Lin Z, McPhail SJ, et al. Continuum scale modelling and complementary experimentation of solid oxide cells. Prog Energy Combust Sci 2021. https://doi.org/10.1016/J.PECS.2020.100902
[9] Zhang S, Hess S, Marschall H, Reimer U, Beale S, Lehnert W. openFuelCell2: A new computational tool for fuel cells, electrolyzers, and other electrochemical devices and processes. Comput Phys Commun 2024. https://doi.org/10.1016/J.CPC.2024.109092
[10] Peters R, Tiedemann W, Hoven I, Deja R, Kruse N, Fang Q, et al. Experimental results of a 10/40 kW-class reversible solid oxide cell demonstration system at Forschungszentrum Jülich. J Electrochem Soc 2023;170(4):044509. https://doi.org/10.1149/1945-7111/accbf0. https://dx.doi.org/10.1149/1945-7111/accbf0
[11] Peters R, Frank M, Tiedemann W, Hoven I, Deja R, Kruse N, et al. Long-term Experience with a 5/15kW-Class reversible solid oxide cell system. J Electrochem Soc 2021;168(1):014508. https://doi.org/10.1149/1945-7111/abdc79
[12] Blum L, Fang Q, De Haart LGJ, Malzbender J, Margaritis N, Menzler NH, et al. Forschungszentrum Jülich–Progress in SOC Development. ECS Trans 2019;91(1):2443.
[13] Kruse N, Tiedemann W, Hoven I, Deja R, Peters R, Blum L, et al. Experimental investigation of efficiency maximization in solid oxide electrolysis systems by internal steam and heat recovery. ECS Trans 2021;103(1):555. https://doi.org/10.1149/10301.0555ecst
[14] Kruse N, Tiedemann W, Hoven I, Deja R, Peters R, Kunz F, et al. Design and experimental investigation of temperature control for a 10 kW SOFC system based on an artificial neuronal network. ECS Trans 2023;111(6):493. https://doi.org/10.1149/11106.0493ecst
[15] Peters R, Deja R, Fang Q, Nguyen VN, Preuster P, Blum L, et al. A solid oxide fuel cell operating on liquid organic hydrogen carrier-based hydrogen – a kinetic model of the hydrogen release unit and system performance. Int J Hydrogen Energy 2019;44(26):13794–806. https://doi.org/10.1016/j.ijhydene.2019.03.220
[16] Peters R, Tiedemann W, Hoven I, Deja R, Kruse N, Fang Q, et al. Development of a 10/40kW-Class reversible solid oxide cell system at Forschungszentrum Jülich. ECS Trans 2021;103(1):289. https://doi.org/10.1149/10301.0289ecst
[17] Yu S, Zhang S, Schäfer D, Peters R, Kunz F, Eichel R-A. Numerical modeling and simulation of the solid oxide cell stacks and metal interconnect Oxidation with openfoam. Energies 2023;16(9):3827. https://doi.org/10.3390/en16093827
[18] Yu S, Schäfer D, Zhang S, Peters R, Kunz F, Eichel R-A. A three-dimensional time-dependent model of the degradation Caused by chromium Poisoning in a solid oxide fuel cell stack. Energies 2023;16(23):7841. https://doi.org/10.3390/en16237841
[19] Al-Masri A, Peksen M, Blum L, Stolten D. A 3D CFD model for predicting the temperature distribution in a full scale APU SOFC short stack under transient operating conditions. Appl Energy 2014;135:539–47. https://doi.org/10.1016/j.apenergy.2014.08.052
[20] Peksen M. 3D transient multiphysics modelling of a complete high temperature fuel cell system using coupled CFD and FEM. Int J Hydrogen Energy 2014;39(10):5137–47. https://doi.org/10.1016/j.ijhydene.2014.01.063
[21] Peksen M. Safe heating-up of a full scale SOFC system using 3D multiphysics modelling optimisation. Int J Hydrogen Energy 2018;43(1):354–62. https://doi.org/10.1016/j.ijhydene.2017.11.026
[22] Navasa M, Miao X-Y, Frandsen HL. A fully-homogenized multiphysics model for a reversible solid oxide cell stack. Int J Hydrogen Energy 2019. https://doi.org/10.1016/J.IJHYDENE.2019.06.077
[23] Rizvandi OB, Miao X-Y, Frandsen HL. Multiscale modeling of degradation of full solid oxide fuel cell stacks. Int J Hydrogen Energy 2021. https://doi.org/10.1016/J.IJHYDENE.2021.05.204
[24] Wehrle L, Schmider D, Dailly J, Banerjee A, Deutschmann O. Benchmarking solid oxide electrolysis cell-stacks for industrial power-to-Methane systems via hierarchical multi-scale modelling. Appl Energy 2022;317:119143. https://doi.org/10.1016/j.apenergy.2022.119143
[25] Zhang X, Wu M, Xiao L, Wang H, Liu Y, Ou D, et al. Thermal stress in full-size solid oxide fuel cell stacks by multi-physics modeling. Energies 2024;17(9):2025. https://doi.org/10.3390/en17092025
[26] Rizvandi OB, Nemati A, Chen M, Frandsen HL. A numerical investigation of nitridation in solid oxide fuel cell stacks operated with ammonia. Int J Hydrogen Energy 2024;50:961–76. https://doi.org/10.1016/j.ijhydene.2023.09.241
[27] Rizvandi OB, Nemati A, Frandsen HL. A numerical study of fuel recirculation in ammonia-fueled solid oxide fuel cell stacks. Int J Hydrogen Energy 2024;53:792–806. https://doi.org/10.1016/j.ijhydene.2023.12.139
[28] Wehrle L, Ashar A, Deutschmann O, Braun RJ. Evaluating high power density, direct-ammonia SOFC stacks for decarbonizing heavy-duty transportation applications. Appl Energy 2024;372:123646. https://doi.org/10.1016/j.apenergy.2024.123646
[29] Chi Y, Lin J, Li P, Song Y. Investigating the performance of a solid oxide electrolyzer multi-stack module with a multiphysics homogenized model. J Power Sources 2024;594:234019. https://doi.org/10.1016/j.jpowsour.2023.234019
[30] Beale SB, Zhubrin SV. A distributed resistance analogy for solid oxide fuel cells. Numer Heat Transfer B Fundament 2005;47:573–91. https://doi.org/10.1080/10407790590907930
[31] Nishida RT, Beale SB, Pharoah JG. Comprehensive computational fluid dynamics model of solid oxide fuel cell stacks. Int J Hydrogen Energy 2016;41:20592–605. https://doi.org/10.1016/j.ijhydene.2016.05.103
[32] Nishida RT, Beale S, Pharoah JG, de Haart LGJ, Blum L. Three-dimensional computational fluid dynamics modelling and experimental validation of the Jülich mark-F solid oxide fuel cell stack. J Power Sources 2018. https://doi.org/10.1016/J.JPOWSOUR.2017.10.030
[33] Zhang S, Peters R, Varghese B, Deja R, Kruse N, Beale SB, et al. Modeling of reversible solid oxide cell stacks with an open-source Library. J Electrochem Soc 2022;169(11):114501. https://doi.org/10.1149/1945-7111/ac9c32
[34] Beale SB, Zhang S, Kulikovsky AA Analytical considerations for hydraulic resistance models of the flow in electrochemical cells. J Electrochem Soc 2025;172(5):054503. https://doi.org/10.1149/1945-7111/add183
[35] Yang C, Li Z, Jin Y, Wang Y, Wu Y, Miao H, et al. Modeling and analysis of the multiphysics transport parameters of a kilowatt-class multistack module of reversible solid oxide cells. Appl Therm Eng 2023;235:121373. https://doi.org/10.1016/j.applthermaleng.2023.121373
[36] Beale SB. Calculation procedure for mass transfer in fuel cells. J Power Sources 2004;128:185–92. https://doi.org/10.1016/j.jpowsour.2003.09.053
[37] Beale SB. Mass transfer formulation for polymer electrolyte membrane fuel cell cathode. Int J Hydrogen Energy 2015;40:11641–50. https://doi.org/10.1016/j.ijhydene.2015.05.074. http://www.sciencedirect.com/science/article/pii/S036031991501232X
[38] Patankar SV, Spalding DB. A calculation procedure for the transient and steady-state behaviour of shell-and-tube heat exchangers. Imperial College of Science and Technology, Department of Mechanical Engineering; 1972.
[39] Peksen M, Peters R, Blum L, Stolten D. Hierarchical 3D multiphysics modelling in the design and optimisation of SOFC system components. Int J Hydrogen Energy 2011;36(7):4400–8. https://doi.org/10.1016/j.ijhydene.2010.12.122.
[40] Howell JR, Mengüç MP, Daun K, Siegel R. Thermal radiation heat transfer. CRC press; 2020.
[41] Zhang S, Yu S, Peters R, Beale SB, Marschall H, Kunz F, et al. A new procedure for rapid convergence in numerical performance calculations of electrochemical cells. Electrochimica Acta 2023. https://doi.org/10.1016/J.ELECTACTA.2023.143275
[42] Nguyen VN, Fang Q, Packbier U, Blum L. Long-term tests of a Jülich planar short stack with reversible solid oxide cells in both fuel cell and electrolysis modes. Int J Hydrogen Energy 2013;38(11):4281–90. https://doi.org/10.1016/j.ijhydene.2013.01.192
[43] Fang Q, de Haart U, Schäfer D, Thaler F, Rangel-Hernandez V, Peters R, et al. Degradation analysis of an SOFC short stack Subject to 10, 000 h of operation. J Electrochem Soc 2020;167(14):144508. https://doi.org/10.1149/1945-7111/abc843
[44] Vibhu V, Yildiz S, Vinke IC, Eichel R-A, Bassat J-M, De Haart LGJ. High performance LSC infiltrated LSCF oxygen electrode for high temperature steam electrolysis application. J Electrochem Soc 2019;166(2):102–8. https://doi.org/10.1149/2.0741902jes. https://iopscience.iop.org/article/10.1149/2.0741902jes
[45] Blum L, Fang Q, Gross-Barsnick SM, de Haart LGJB, Malzbender J, Menzler NH, et al. Long-term operation of solid oxide fuel cells and preliminary findings on accelerated testing. Int J Hydrogen Energy 2020;45(15):8955–64.
[46] Fang Q, Haart UD, Schäfer D, Thaler F, Rangel-Hernandez V, Peters R, et al. Degradation analysis of an SOFC short stack subject to 10, 000 h of operation.

J Electrochem Soc 2020;167(14):144508. https://doi.org/10.1149/1945-7111/abc843

[47] Selmert V, Paschalidis L, Kruse N, Dirkes S, Kretzschmar A, Jerome G, et al. Overcoming the energy–water nexus in dry regions – water-positive production of green hydrogen carriers and base chemicals: the DryHy project – technical aspects. Sustain Energy Fuels 2025;9(7):1672–82. https://doi.org/10.1039/D4SE01783H. https://xlink.rsc.org/?DOI=D4SE01783H

[48] Damm DL, Fedorov AG. Radiation heat transfer in SOFC materials and components. J Power Sources 2005;143(1):158–65. https://doi.org/10.1016/j.jpowsour.2004.11.063

[49] Daun KJ, Beale SB, Liu F, Smallwood GJ. Radiation heat transfer in planar SOFC electrolytes. J Power Sources 2006;157(1):302–10. https://doi.org/10.1016/j.jpowsour.2005.07.045

[50] Akhtar N, Decent SP, Kendall K. Numerical modelling of methane-powered micro-tubular, single-chamber solid oxide fuel cell. J Power Sources 2010;195(23):7796–807. https://doi.org/10.1016/j.jpowsour.2010.01.084

[51] Bao C, Cai N, Croiset E. An analytical model of view factors for radiation heat transfer in planar and tubular solid oxide fuel cells. J Power Sources 2011;196(6):3223–32. https://doi.org/10.1016/j.jpowsour.2010.11.128